Deep Surrogates for Finance: With an Application to Option Pricing

Hui Chen Antoine Didisheim Simon Scheidegger*

January 29, 2025

Abstract

We introduce "deep surrogates" – high-precision approximations of structural models based on deep neural networks, which speed up model evaluation and estimation by orders of magnitude and allow for various compute-intensive applications that were previously infeasible. As an application, we build a deep surrogate for a high-dimensional workhorse option pricing model. The surrogate enables us to re-estimate the model at high frequency to construct an option-implied tail risk measure, which is highly predictive of future market crashes. It also helps us systematically examine the model's out-of-sample performances, which reveals the tradeoffs between structural and reduced-form approaches for option pricing. Moreover, we construct a measure for the degree of parameter instability and connect it to option market illiquidity in the data. Finally, we use the surrogate to construct conditional distributions of option returns, which is useful for risk management and provides a new way to test the model.

Keywords: surrogate, deep neural network, tail risk index, parameter instability, illiquidity, distribution of option return

*Chen: MIT Sloan and NBER. Email: huichen@mit.edu. Didisheim: Department of Finance, HEC Lausanne, University of Lausanne and Swiss Finance Institute. Email: antoine.didisheim@unil. Scheidegger: Department of Economics, HEC Lausanne, University of Lausanne and Enterprise for Society. Email: simon.scheidegger@unil. We thank Dimitris Papanikolaou (the editor) and an anonymous referee for their insightful comments. We also thank Lorenzo Bretscher, Xiaohong Chen, Mathieu Fournier, Bryan Kelly, Andrew Lo, Semyon Malamud, John Rust, Olivier Scaillet, Fabio Trojani, seminar participants at the University of Geneva, the University of Lausanne, MIT, and participants of the 2021 CICF, the 2021 Econometrics Society Winter Meeting, the SIAM conference 2021, the PASC 2021 conference, the Econometric Society Summer School and Conference 2021 at Bonn, and the Econometric Society Summer School and Conference at Lausanne for comments. This work is generously supported by grants from the Swiss National Supercomputing Center (CSCS) under project ID 995, and the Swiss National Science Foundation under project IDs "Can Economic Policy Mitigate Climate-Change?," and "New methods for asset pricing with frictions." The trained surrogate for this paper is available at: https://github.com/DeepSurrogate/OptionPricing.

1 Introduction

Driven by advances in theory and the availability of "big data," contemporary models in economics are becoming increasingly complex. State-of-the-art structural models often impose a substantial roadblock to researchers as they increasingly suffer from the curse of dimensionality, that is, the computational burden grows exponentially with every additional degree of freedom. The problem is exacerbated in analyses necessitating numerous model evaluations. This is particularly evident in cases such as Bayesian estimation of DSGE models, out-of-sample analysis with time-varying model parameters, and the estimation of heterogeneity within a large cross-section of households using a life-cycle model.

To tackle these challenges, we introduce *deep surrogates*, a new framework to evaluate and estimate structural models. Conceptually, our method re-purposes the concept of surrogate models commonly applied in physics and engineering for the context of economic models. By taking advantage of the strong approximating power of deep neural networks (DNN), one can create high-precision surrogates for high-dimensional models, which take the same input from the original model, including both the states and model parameters, and produce the same output at a significantly lower computational cost. Furthermore, the gradient of the deep surrogate can be computed efficiently via automatic differentiation, which is particularly helpful for model estimation. Simply put, the surrogate is a high-dimensional look-up table. Once built, it is fast to use, easy to share and build on, and avoids the cost and uncertainty of individual replications.

To build a deep surrogate for a structural model, we first generate a sufficiently representative training sample by evaluating the original model and collecting the relevant output at different locations in the input space and then train a neural network to minimize the fitting errors in the training sample. Generating a training sample of sufficient size to ensure approximation accuracy across the input space is the main bottleneck for building the surrogate. To improve the efficiency of surrogate building, we propose an iterative procedure that alternates between surrogate training and validation. Both the training sample size and network complexity will grow in the process until the desired level of approximation accuracy is reached.

Deep neural networks are uniquely suitable for our task due to two theoretical reasons. First, the strong approximation power of DNNs is formally established by the universal approximation theorem (see e.g., Hornik, Stinchcombe, and White, 1989; Hanin, 2019). DNNs have also been shown to be able to achieve high accuracy with a relatively simple network structure (as measured by the total number of trainable parameters) and modest training sample size.[1] Intuitively, provided that the target function is sufficiently smooth and is from a bounded domain, and the training examples are reasonably well scattered across the domain, a neural network is capable of "learning" its features with a relatively small number of examples. For example, for a popular class of affine option pricing models, the training sample needed is shown to only grow polynomially in the dimension of the input (see Grohs et al., 2023; Berner, Grohs, and Jentzen, 2020).[2] This is in clear contrast to traditional grid-based approximation methods, where the required grid points grow exponentially in input dimension. In that case, even when a single function evaluation is relatively inexpensive, approximation of a high-dimensional function in this way can quickly become infeasible.

Second, the risks of overfitting are low when training a deep surrogate because we know the true data-generating process and can generate an arbitrarily large training sample with high signal-to-noise ratio. For example, in an option pricing model, we know what the relevant features are (no missing features) and how the option price depends on the features (no unspecified randomness). Thus, when we generate training data, there is no irreducible error in theory. As a result, while we use a relatively large neural network, we can train it for a large number of epochs without network shrinkage, dropout, or early stopping (see, e.g., Goodfellow et al. (2016)).

We apply the deep surrogate methodology to study a workhorse option pricing model, a double-exponential jump-diffusion model with stochastic volatility. Since it is a direct extension of Bates (1996) (who considers log-normally distributed jumps), we refer to it as the "Bates model" for simplicity. The model features 13 states and parameters. Using the iterative training procedure, during which the depth of the network and the size of

[1] See Gühring, Raslan, and Kutyniok (2020) for a recent survey on the large body of work of approximation results for deep neural networks.

[2] Neural networks have also been shown to alleviate or break the curse of dimensionality for compositional or polynomial functions (Bach, 2017; Petersen and Voigtlaender, 2018), functions in the Korobov spaces (Montanelli and Du, 2019), and generalized bandlimited functions (Montanelli, Yang, and Du, 2021).

the training sample grow gradually, we achieve the desired approximation accuracy with a network of 7 hidden layers and nearly a million parameters. The final training sample size is 10^9, which is highly sparse considering the dimensionality of the input space ($d = 13$). We verify through simulation that the deep surrogate not only prices options and produces the greeks accurately but can also accurately identify the structural parameters in Generalized Method of Moments (GMM) estimations. Moreover, it helps reduce the average time for estimating the model parameters by orders of magnitude.

The deep surrogate enables us to carry out a variety of analyses that would have incurred prohibitive computation costs otherwise. By re-estimating the model parameters daily, we are able to i) construct a high-frequency option-implied tail risk index for the stock market, ii) quantify the time variation in the degree of parameter instability and study its implications for option market liquidity, and iii) systematically examine the out-of-sample performances of the Bates model. Finally, the surrogate enables us to efficiently characterize the model-implied conditional distributions of option returns, which can be tested in the data.

First, through the daily re-estimation of the Bates model, we recover unique information about the stock market as conveyed by the options market. These include the time variation in the correlation between changes in stock price and instantaneous variance, also known as the "leverage effect," as well as the asymmetry between upward and downward jump risks in the market. We construct a daily tail risk index using the estimated parameters, $TailRisk$, which measures the risk-neutral expected loss due to a negative jump in the market index over the next week. We show that $TailRisk$ has strong predictive power for actual tail events in the market. For example, whether defining the tail event as "a cumulative loss 10% or more in the S&P 500 over the next 5 days" or as "a daily drop of 5% or more in the S&P 500 for any of the next 5 days," the Pseudo-R^2 coefficient in a logistic regression almost doubles with $TailRisk$ compared to with the non-parametric option-based left-tail probability measure from Bollerslev, Todorov, and Xu (2015).

Next, we examine parameter stability for the Bates model. Using the statistical test proposed by Andersen, Fusari, and Todorov (2015), we construct a parameter instability measure using the GMM estimators for model parameters at daily frequency. The measure reveals the severity of parameter instability for the Bates model: we reject the hypothesis

that the parameter values are the same from two adjacent days 41.6% of the time (at the 1% significance level).

Furthermore, we examine the potential economic repercussions of parameter instability within option pricing models for option market liquidity. When these models become more unstable, the ability of option market makers to accurately hedge the risks of their inventories diminishes, which could in turn diminish their risk appetite and reduce market liquidity. Consistent with this prediction, we find a positive and statistically significant relation between the degree of parameter instability and relative bid-ask spreads for the SPX options. The coefficient for parameter instability remains significantly positive after controlling for contract fixed effect, contract level abnormal volume, time-to-maturity, and moneyness.

Third, we examine the out-of-sample performance of the Bates model and compare it against a reduced-form benchmark, which models the implied volatility surface using random forests (Breiman, 2001), which we refer to as the "RF model." This comparison helps us better understand the relative advantages of structural vs. reduced-form approach for option pricing. Conceptually, structural models could help guard against over-fitting by imposing restrictions between the dynamics of option prices and the underlying states, but they likely suffer from misspecification due to a lack of flexibility as well as abstractions from various factors due to tractability concerns. However, it can be difficult to thoroughly examine the out-of-sample performance of a structural model, because one needs to frequently update the parameters (typically by re-estimating them in a moving or expanding window) to capture potential parameter changes while avoiding any look-ahead bias. The deep surrogate substantially alleviates this problem.

Our empirical results confirm an interesting tradeoff between the structural and reduced-form approach for option pricing. The Bates model under-performs the RF for shorter-dated options (with days-to-maturity of 7 days or less) across different moneyness but outperforms the latter for longer-dated options (with days-to-maturity longer than 90 days). Moreover, the relative performance of the Bates model is stronger for near-the-money options and options with lower bid-ask spreads. Such variation in performances between the structural and reduced-form models can be attributed to the varying degrees of misspecification of the structural model. Short-dated options, out-of-the-money options, and options with high

bid-ask spreads are more sensitive to liquidity factors, demand factors, and specific types of jump dynamics that the Bates model does not incorporate. Instead, the Bates model is better suited for capturing fundamental risk exposures in longer-dated options.

The Bates model's relative performance also improves when market volatility or the risk of jumps rises from the training period to the time of forecast, or when an option has strike and time-to-maturity that are further away from the mass of the training sample. Intuitively, since interpolation (extrapolation) by the non-parametric volatility surface becomes less reliable near (outside) the boundaries of the training data domain, the RF model's performance deteriorates in such cases. Taken together, these results suggest that reduced-form models tend to perform better relative to structural models when the latter are more severely misspecified, but they suffer from poor generalizablity beyond the training data.

Finally, we apply the surrogate technology to construct the conditional distribution of option returns. Following the methodology of Israelov and Kelly (2017), we estimate a vector autoregression (VAR) for the relevant states, construct a distribution of future states via bootstrapping, and then use the surrogate to efficiently compute option prices along the different paths. We confront the model-implied conditional return distribution, in particular its quantile forecasts, with the data. The test helps reveal clear advantages of the Bates model over the Heston model (which does not feature jumps) in matching the return distribution.

Related Literature

Our paper contributes to three strands of literature: (i) methods for constructing surrogate models in general and their application to high-dimensional models in economics and finance; (ii) applications of deep learning in finance and economics; and (iii) empirical option pricing.

Model estimation, calibration, and uncertainty quantification can be daunting numerical tasks because of the need to perform a large number of model evaluations to obtain converging estimates of the relevant parameters and converging statistics (see, e.g., the survey by Fernández-Villaverde, Rubio-Ramírez, and Schorfheide, 2016). To this end, a broad strand of literature in engineering, physics (see, e.g., Tripathy and Bilionis, 2018),[3] as well as finance

[3]In physics and engineering, Gaussian processes regression (see, e.g., Williams and Rasmussen, 2006; Tripathy, Bilionis, and Gonzalez, 2016; Chen, Zabaras, and Bilionis, 2015), radial basis functions (Park and

and economics has long tried to replace expensive model evaluations that suffer from the curse of dimensionality with cheap-to-evaluate surrogate models that mitigate the said curse. Heiss and Winschel (2008) for instance, approximate the likelihood by numerical integration on Smolyak sparse grids, whereas Scheidegger and Treccani (2018) apply adaptive sparse grids to approximate high-dimensional probability density functions (PDFs) in the context of American option pricing. Scheidegger and Bilionis (2019) propose a Gaussian process-based method to carry out uncertainty quantification in the context of discrete-time dynamic stochastic models. Kaji, Manresa, and Pouliot (2020) propose a simulation-based estimation method for structural models in economics using a generative adversarial neural network. Norets (2012) extends the state-space by adding the model parameters as "pseudo-states" to estimate finite-horizon, dynamic discrete choice models. A recent, notable contribution in this area is by Kase, Melosi, and Rottner (2022), who estimate a HANK model by approximating the likelihood function via neural network surrogates, building on previous work by Maliar, Maliar, and Winant (2021).

To the best of our knowledge, we are the first to show that *Swish* activation function (Ramachandran, Zoph, and Le, 2017) are superior to the well-known alternatives, *sigmoid* and $ReLU$, when constructing high-dimensional surrogate to approximate and estimate complex structural models. The *sigmoid* activation suffers from the vanishing gradient problem (Hochreiter, 1998), which can prohibit the use of networks that are sufficiently deep to accurately approximate complicated functions. The $ReLU$ activation function, on the other hand, is not differentiable at zero. As a result, while a surrogate with $ReLU$ activation may attain approximation accuracy comparable to that of one with *Swish* activation, it is prone to producing larger errors in function gradients, which would significantly diminish its accuracy in parameter estimation (due to the fact the gradients are essential inputs to a variety of extreme estimators).

Secondly, our paper is part of the emergent literature on the applications of deep learning to economics and finance, where shallow and deep neural networks are used, for instance, in

Sandberg, 1991), or relevance vector machines (Bilionis and Zabaras, 2012) are often used to build surrogate models. More recently, following the rapid developments in the theory of stochastic optimization and artificial intelligence as well as the advances in computer hardware leading to the widespread availability of graphic processing units (GPUs; see, e.g., Scheidegger et al. (2018); Aldrich et al. (2011), and references therein), researchers have turned their attention towards *deep neural networks* (see, e.g., Liu et al., 2019).

the context of asset pricing and econometric tasks (see, e.g., Hutchinson, Lo, and Poggio, 1994; Chen and White, 1999; Farrell, Liang, and Misra, 2021; Chen, Pelger, and Zhu, 2023; Chen et al., 2024), and to solve a broad range of high-dimensional dynamic stochastic models in discrete and continuous-time settings, but do not directly deal with estimation.[4]

Thirdly, in the option pricing application, the deep surrogate allows us to efficiently re-estimate the structural parameters and hidden states at high frequency. In recent work, Gao and Pan (2023) construct an option-implied crash index by estimating the model from Pan (2002). They find that changes in their crash index negatively predicts future market returns. Christoffersen and Jacobs (2004) compare the pricing performance of a reduced-form "Practitioner's Black-Scholes model" against the Heston model and find that the reduced-form model outperforms the Heston model out of sample. We show that structural option pricing models could outperform reduced-form models in settings where model misspecification is less severe and generalizablity is important. It echoes the finding of Schaefer and Strebulaev (2008) in the corporate bond market, which shows that structural credit models are informative about out-of-sample hedge ratios.

The remainder of this paper is organized as follows. In Section 2, we present the *deep surrogate* methodology and discuss how to apply it to option pricing models. Section 3 presents the applications. In Section 4, we confront our methodology in the context of real data. Section 5 concludes.

2 Methodology

In this section, we first introduce the deep surrogate methodology. Then, we compare deep neural networks with other methods in the context of surrogate models.

[4]For an incomplete list of research, see, e.g., Maliar, Maliar, and Winant (2021); Azinovic, Gaegauf, and Scheidegger (2022); Fernández-Villaverde, Hurtado, and Nuño (2023); Duarte, Duarte, and Silva (2023); Friedl et al. (2023); Han, Yang et al. (2021); Payne, Rebei, and Yang (2024); Villa and Valaitis (2019), among others.

2.1 Deep Surrogates

Consider an economic model that maps state variables $s \in \mathbb{R}^n$ into policies (e.g., consumption or investment), equilibrium prices and quantities, or their moments, which are summarized by $y \in \mathbb{R}^k$. We represent the mapping with the function

$$y = f(s|\theta), \tag{1}$$

where $\theta \in \mathbb{R}^p$ is the vector of model parameters. By treating the parameters θ as pseudo-states, we can define the augmented states $x \equiv [s, \theta]$, with $x \in \mathbb{R}^d$, $d = n + p$, and rewrite (1) as $y = f(x)$. Following the terminology of machine learning theory, we denote the admissible input and target space for f by $\mathcal{X}$ and $\mathcal{Y}$, respectively.

In situations where the function f is computationally expensive to evaluate, one may wish to build a cheap-to-evaluate surrogate, $\widehat{f}$, for the original function f. A familiar example of such a surrogate is the standard normal table, which stores pre-computed values for the CDF function of the standard normal distribution on a grid. We propose to use deep neural networks (DNNs) to construct the said surrogate, which we refer to as *deep surrogate*.

Treating the parameters as pseudo-states has the benefit in that we can build one surrogate to capture the mapping between s and y under different model parameterizations. Since doing so further increases the dimensionality of the problem, it is vital that the class of functions we use to build a surrogate is sufficiently flexible (high expressivity) to approximate the original function accurately. Moreover, the process of building the surrogate should not be prohibitively expensive, for example, with the number of function evaluations required growing exponentially with the dimensionality as in the case of Cartesian grid-based methods. As we explain below, for a large class of functions which occur in economics, deep neural networks meet both requirements.

Before explaining the procedure for constructing a deep surrogate, we briefly outline the key elements of a basic type of deep neural networks called feedforward networks. These networks consist of multiple stacked-up layers of neurons. A given layer ℓ takes a vector

$x^{[\ell-1]}$ as input and produces a vector $x^{[\ell]}$ as output,

$$x^{[\ell]} = \sigma\left(W_\ell x^{[\ell-1]} + b_\ell\right), \tag{2}$$

where W_ℓ and b_ℓ are parameters for the network; $\sigma(\cdot)$ is a non-linear function applied element-wise and is commonly termed an *activation function*.[5] For a neural network with L layers, $x^{[0]}$ represents the network's inputs, and $x^{[L]}$ represents the final output. Denote the dimension of $x^{[\ell]}$ by a_ℓ. Then, one can characterize a network with activation function σ, architecture of the network $a = (a_0, \cdots, a_L)$, and parameters $\phi = ((W_\ell, b_\ell))_{\ell=1}^{L}$.

The objective of a surrogate is to take any augmented state vector $x \in \mathcal{X}$ as input and produce $\widehat{f}(x)$ that is as close to the target $y = f(x)$ as possible based on some metric. Given a loss function $\mathcal{L} : \mathcal{Y} \times \mathcal{Y} \to [0, \infty]$, we aim to find a function $\widehat{f}$ that minimizes the expected loss of approximation $E\left[\mathcal{L}(\widehat{f}(x), y)\right]$, where the expectation is over the joint distribution of x and y. When training a deep surrogate, we look for $\widehat{f}$ within the class of neural networks $\mathcal{H}$, and replace the expectation by the empirical loss over a sample (training set) $\mathcal{S} = ((x_i, y_i))_{i=1}^{m}$ drawn from $\mathcal{X} \times \mathcal{Y}$,

$$\widehat{f}_{\mathcal{H},\mathcal{S}} = \arg\min \left\{ \frac{1}{m} \sum_{i=1}^{m} \mathcal{L}(\widehat{f}(x_i), y_i) : \widehat{f} \in \mathcal{H} \right\}. \tag{3}$$

Different from typical machine learning applications, where the data-generating process is unknown, we know the true f from the economic model and can generate as much data as desired (allowed by the computing budget). However, this is usually the most compute-intensive step in building a deep surrogate, because the original function is costly to evaluate (hence the need for a surrogate) and the size of the sample required for training a neural network of sufficient accuracy is large. With this mind, we now describe the steps for training a deep surrogate.

Generating the training sample. We obtain random draws $\tilde{x}_i$ from the input space $\mathcal{X}$ as follows. Assume $\mathcal{X}$ is a hypercube. For each element $x_t^{(j)}$ in x_t, let $\underline{x}^{(j)}$ and $\bar{x}^{(j)}$ be it's

[5] Popular choices for the activation function include the sigmoid function and rectified linear unit (ReLU).

lower bound and upper bound, respectively, and

$$\underline{x} = [\underline{x}^{(1)}, \underline{x}^{(2)}, \cdots, \underline{x}^{(m)}], \quad \overline{x} = [\bar{x}^{(1)}, \bar{x}^{(2)}, \cdots, \bar{x}^{(m)}]. \tag{4}$$

We then draw $\tilde{x}_i$ according to:

$$\tilde{x}_i = \underline{x} + \tilde{R}_i(\bar{x} - \underline{x}), \tag{5}$$

where $\tilde{R}_i = \text{diag}(\tilde{r}_i)$, with $\tilde{r}_i \in \mathbb{R}^m$ following an appropriate multivariate distribution. One possibility is to first impose a hierarchical prior on parameters θ, and then draw x according to the conditional distribution implied by the model. Alternatively, one can use the multivariate uniform distribution, which overweights the states that are relatively rarely visited in the model. Yet another possibility is to oversample the regions of the input space where the function is highly nonlinear or where the approximation error is large.

For each x_i drawn, we compute $y_i = f(x_i)$ using the true f. The resulting training sample is $\mathcal{S} = ((x_i, y_i))_{i=1}^m$.

Surrogate training. Next, we train the deep surrogate $\widehat{f}_{\mathcal{H},\mathcal{S}}$ over the sample $\mathcal{S}$. For a given architecture (the depth L and the width of each layer a_ℓ), this amounts to searching for network parameters ϕ to minimize the empirical loss in (3). For our application, we will use the ℓ_1-norm between the prediction of the surrogate and the target as the loss function, which is simply the mean-absolute error when the dimension of the target y is $k = 1$.

We perform the minimization in (3) using stochastic gradient descent and the back-propagation algorithm. In standard machine learning applications, the stochastic gradient descent is typically stopped before convergence (known as "early stopping") to reduce the risks of over-fitting. In contrast, we can train a deep surrogate for a large number of epochs without network shrinkage, dropout, or early stopping. This is thanks to two unique features of building a surrogate: (i) high signal-to-noise ratio of the training data – the target y_i is (essentially) noise-free (limited to the numerical errors when evaluating the original function f), and (ii) we can increase the size of the training sample as desired with knowledge of the

true model.[6,7]

Surrogate validation. After training, we evaluate the accuracy of the deep surrogate model $\widehat{f}(x|\phi^*)$, where ϕ^* are the optimal parameters found during the training of the surrogate. Since it is important that the approximation of the surrogate is accurate in different parts of the input space, not just on average, we propose to use the following acceptance criterion:

$$\sup_{x\in\mathcal{X}} \mathcal{L}\left(\widehat{f}(x|\phi^*), f(x)\right) \leqslant \varepsilon, \tag{6}$$

where ε is some small positive constant. This means that the approximation error of the surrogate, as measured by the loss function $\mathcal{L}$, needs to be bounded globally.

To implement (6), we generate a new sample of size N as validation set, $\mathcal{V} = \left(x_j^o, y_j^o\right)_{j=1}^N$, and evaluate the condition

$$\sup_{j} \mathcal{L}\left(\widehat{f}(x_j^o|\phi^*), f(x_j^o)\right) \leqslant \varepsilon, \tag{7}$$

If Condition (7) is satisfied, our training of the deep surrogate is finished. Otherwise, we can add flexibility to $\widehat{f}$ by modifying its architecture (e.g., increasing the depth or width), and increase the size of the training sample, especially from regions of the input space where the approximation error is large, to further reduce approximation errors. The latter is a form of active learning, which systematically augments the training set with observations from areas where the model performs poorly (see Ren et al., 2021, for more detaiils). We then re-train and re-validate the model, and we iterate on these steps until Condition (7) is met.

2.2 Benefits of the Deep Surrogate

Having explained the algorithm for building a deep surrogate, we now turn to the advantages that deep neural networks offer relative to conventional function approximation methods.

[6]Figure A.1 in Appendix A uses a deep surrogate for the Black-Scholes model to illustrate that the risks of over-ftting are low.

[7]Additionally, in situations where the size of training sample is small (e.g., because the model solutions are costly to compute), we can still deploy DNNs with trainable parameters potentially exceeding the training sample size and exploit the recently discovered double descent phenomenon (see, e.g., Belkin, Rakhlin, and Tsybakov, 2019; Belkin, Hsu, and Xu, 2020).

The deep surrogate acts as a (high-dimensional) lookup table. Once trained, the evaluation of a deep surrogate can be reduced to a succession of matrix multiplications and the application of activation functions, which is highly parallelizable and is well suited to take advantage of modern hardware such as GPUs. Moreover, thanks to the backward propagation algorithm, we obtain the gradient of a deep surrogate for little to no extra computational costs. This can be particularly useful for model estimation and sensitivity analysis (see, e.g., Chen, Dou, and Kogan, 2022). In section 3.2, we use an option pricing model to illustrate the performance improvement from the deep surrogate.

Upfront vs. recurring cost. In exchange for faster model evaluation, the deep surrogate does require a large upfront cost, including the cost of generating a sizable training sample and training the network. However, this tradeoff is worthwhile for several reasons.

First, while the one-time upfront cost for building the surrogate can be large, it leads to a massive improvement in computing speed in all future model evaluations. Thus, in cases where a large number of model evaluations is needed (e.g., when pricing a large panel of options or performing structural estimation), the benefits of a deep surrogate post-training can easily outweigh the upfront costs.

Second, the main upfront cost is generating the training and validation samples. This process is ideally suitable for parallelization, which can significantly reduce the runtime.

Third, deep surrogate models are highly portable. One only needs to store the parameters for the neural network, which is substantially smaller than the amount of data storage needed when using a grid-based method. This feature makes it easy to share a high-quality deep surrogate among many users (just like the standard normal table), rather than having individual users incurring the cost for solving the model.

Why DNNs? One can build a surrogate model using a variety of function approximators, such as Chebyshev polynomials or splines. Deep neural networks have several desirable properties for our purposes. Following Azinovic, Gaegauf, and Scheidegger (2022), Table 1 offers a comparison of DNN and other standard approximation methods.

First, neural networks are universal function approximators, in that they can approximate any continuous function arbitrarily well (see, e.g., Hornik, Stinchcombe, and White,

Table 1: **A Comparison of Approximation Methods**

This table provides a comparison of different approximation methods. "High-dimensional input" refers to problems with state space dimensions higher than four. "Capturing local features" refers to the ability to deal with strong nonlinearity, such as kinks. "Irregularly-shaped domain" refers to problems with geometries other than a hypercube. "Large amount of data" refers to the ability to deal with more than $10,000$ observations.

	Polynomials	Splines	(Adaptive) sparse grids	Gaussian processes	Deep neural networks
High-dimensional input	✓	✗	✓	✓	✓
Capturing local features	✗	✓	✓	✓	✓
Irregularly-shaped domain	✓	✗	✗	✓	✓
Large amount of data	✓	✓	✓	✗	✓

1989; Hanin, 2019). They allow for high-dimensional input, can handle irregularly shaped domains, and can approximate functions with kinks and ridges. In contrast, polynomial-based interpolation, which is popular in economics, have difficulties resolving kinked features.[8] Adaptive sparse grids can approximate functions with local features using a large amount of high-dimensional data but are inefficient on irregular domains (see, e.g., Brumm and Scheidegger, 2017). Gaussian processes can approximate high-dimensional functions on irregularly shaped domains, but become prohibitively slow when using a large amount of data (see, e.g., Traub and Werschulz, 1998; Williams and Rasmussen, 2006), which is often necessary to capture local features.

Second, while the complexity of the network and the size of the training sample required to achieve desired level of approximation accuracy depends on the target function, DNNs can alleviate and sometimes overcome the curse of dimensionality for certain classes of functions. For example, Grohs et al. (2023) and Berner, Grohs, and Jentzen (2020) prove that when approximating the solution to the Black-Scholes PDEs with affine drift and diffusion coefficients, both the number of trainable network parameters and the size of the training sample grow at most polynomially (instead of exponentially) in input dimension. These

[8]To accurately approximate local features, such as kinks, it is essential that the approximating function can fit strong nonlinearities in some areas of the domain without deteriorating the approximation quality in others. Polynomial-based interpolation, which approximates a kinked function by interpolating points with global polynomials, often leads to undesired "wiggles", known as Runge's phenomenon, which occur away from the kink).

theoretical guarantees imply that, in high dimensional settings, one can train high-accuracy deep surrogates with substantially fewer observations than in the case of traditional methods based on Cartesian grids. Notice that the setting considered above is not limited to option pricing. In fact, it is widely applicable in economic modeling thanks to the popularity of affine processes (see e.g., Chen and Joslin, 2012).

A third benefit of DNN is that its Jacobian, $\frac{\partial \hat{f}}{\partial x'}$, is readily available through automatic differentiation (also known as "backpropagation" in the context of neural networks), which can be very helpful for local sensitivity analysis or working with extreme estimators. For example, suppose we want to estimate the model parameters θ using GMM, with the moment conditions implied by Eq. (1) from the economic model. Assuming the system of moment restrictions is over-identified, the GMM estimator for θ with a weighting matrix W is

$$\hat{\theta}_{GMM} = \arg\min_{\theta} g_T(\theta)^T W g_T(\theta), \quad \text{with} \quad g_T(\theta) \equiv \frac{1}{T}\sum_{t=1}^{T}(f(s_t|\theta) - y_t). \tag{8}$$

When we replace $f(s|\theta)$ with a high-precision deep surrogate, $\widehat{f}(x)$, the evaluation of both the GMM objective and its gradient becomes much easier. In fact, the first-order condition to (8) implies a system of non-linear equations, which can be solved efficiently. This is in contrast to having to estimate the gradient through numerical differentiation schemes, which further adds to the large number of costly model evaluations entailed in a typical parameter search.

2.3 Deep Surrogate and Model Misspecification

Since a surrogate function is only an approximation of the true function, substituting the deep surrogate $\widehat{f}(x|\phi^*)$ for the original function $f(x)$ introduces a form of model misspecification. Here, we briefly discuss its consequence for parameter estimation in the context of GMM.

Denote the moment function implied by the structural model as $m(x_i, \theta)$ and the corresponding moment function based on the deep surrogate as $\widehat{m}(x_i, \theta)$. Then,

$$\widehat{m}(x_i, \theta) = m(x_i, \theta) + e(x_i, \theta), \tag{9}$$

where $e(x_i, \theta)$ is the error in $\widehat{m}(x_i, \theta)$ resulting from the approximation errors of the surrogate. Given that our training criterion (6) for the deep surrogate bounds its approximation error globally, the degree of misspecification will also be bounded. This is referred to in the literature as "mild misspecification" (see e.g., Hansen and Lee, 2021).

Under the assumption that the structural model is correctly specified, there exists a unique θ_0 such that $\mathbb{E}[m(x_i, \theta_0)] = 0$. However, the same is not true for $\widehat{m}(x_i, \theta)$. The universal approximation theorem for neural networks ensures that, with a sufficiently flexible neural network (in terms of depth or width) and a sufficiently large training set, the error term $e(x_i, \theta)$ can be made arbitrarily small. However, for any given surrogate, the error $e(x_i, \theta)$ does not become any smaller as the sample size n for the GMM estimation increases. Taken together, it means that the approximation errors of the deep surrogate result in a form of non-local and mild misspecification.

Let us assume that a pseudo-true parameter value θ_* exists, i.e., θ_* minimizes the population version of the GMM J-statistic, $\mathbb{E}[\widehat{m}(x_i, \theta)]' W \mathbb{E}[\widehat{m}(x_i, \theta)]$, where W is a given weighting matrix. Then $\mu^* = \mathbb{E}[\widehat{m}(x_i, \theta_*)]$ can be viewed as the degree of non-local misspecification. Hall and Inoue (2003) show that, under certain regularity conditions, the GMM estimator for a non-locally misspecified model is generally biased and inconsistent; it converges to the pseudo-true parameter value θ_*, and

$$T^{-1/2}\left(\hat{\theta}_T - \theta_*\right) \xrightarrow{d} N\left(0, \Sigma\right), \tag{10}$$

where the asymptotic variance Σ, the expression of which is given in Theorem 1 of Hall and Inoue (2003), depends on the degree of non-local misspecification μ^*. Furthermore, as we keep improving the accuracy of the deep surrogate, the approximation error $e(x_i, \theta)$ converges to zero (based on the universal approximation theorem), θ_* will converge to θ_0. In the limit where $\mu^* = 0$, the asymptotic covariance Σ reduces to the asymptotic variance for the correctly specified model as given by Hansen (1982). Thus, the global bound for the approximation errors of the deep surrogate in (6) is essential for the validity and reliability of surrogate-based inference.

3 Application to Option Pricing

Next, we apply the deep surrogate technology to conduct an in-depth study of a leading option-pricing model. We choose this example for several reasons. Option pricing models are among the most widely applied quantitative models in research and practice, and they can help us extract useful information from the options market. Moreover, as discussed in Section 2.2, there is theoretical guarnatee (e.g., by Berner, Grohs, and Jentzen, 2020) that the solutions to affine option pricing models are particularly suitable to be approximated by DNNs. In this section, we build the surrogate and analyze its performance.

3.1 The Bates Model

The example we choose to illustrate the deep surrogate methodology is an extended version of the model of Bates (1996). This is a workhorse model that features stochastic volatility and jumps in the underlying asset, and we replace the original assumption of normal distribution for the log jump size with an asymmetric double-exponential distribution, which is an important feature in the data. While the deep surrogate methodology can be readily applied to more sophisticated models (for example, Duffie, Pan, and Singleton, 2000; Bates, 2000; Pan, 2002; Andersen, Fusari, and Todorov, 2015), we choose this example for a balance between transparency and complexity.

Under the risk-neutral measure $\mathbb{Q}$, the stock price S_t and the conditional variance v_t follow the process

$$dS_t = (r_t - d_t - \lambda\bar{\nu})S_t dt + S_t\sqrt{v_t}dW_t^s + d\left(\sum_{j=1}^{N_t} S_{t^-}\left(e^{Z_j} - 1\right)\right), \tag{11a}$$

$$dv_t = \kappa(\bar{v} - v_t)dt + \sigma\sqrt{v}dW_t^v, \tag{11b}$$

where r is the instantaneous risk-free rate and d is the dividend yield. The conditional variance v_t follows a Feller process, with the speed of mean reversion κ, long-run mean $\bar{v}$, and volatility parameter σ. The two standard Brownian motions under $\mathbb{Q}$, W_t^s and W_t^v, are correlated with $\mathbb{E}^{\mathbb{Q}}[dW_t^s dW_t^v] = \rho dt$. Finally, N is a Poisson process with constant arrival

intensity λ, and Z_j follows a double-exponential distribution with density

$$f_Z(z) = p\frac{1}{\nu_u}e^{-\frac{z}{\nu_u}}1_{\{z>0\}} + (1-p)\frac{1}{\nu_d}e^{\frac{z}{\nu_d}}1_{\{z<0\}}, \tag{12}$$

where $0 < \nu_u < 1$, $\nu_d > 0$, and $0 \leqslant p \leqslant 1$ is the probability of a positive jump conditional on having a jump. The average jump size is $\bar{\nu} \equiv \frac{p}{1-\nu_u} + \frac{1-p}{1+\nu_d} - 1$. The double-exponential assumption allows for heavier tails in jumps than the normal distribution as well as more flexibility to capture the asymmetry between positive and downward jumps, features supported by the evidence in Bollerslev and Todorov (2011).

A European option with maturity T and strike price K can be priced as the expected payoff under $\mathbb{Q}$ discounted using the risk-free rate. The price of a European call option at time t is

$$C(S_t, t, v_t) \equiv E^{\mathbb{Q}}[e^{-r(T-t)}(S_T - K)^+]. \tag{13}$$

The solution can be obtained through Fourier inversion of the characteristic function for affine processes (see Duffie, Pan, and Singleton, 2000).[9] Thanks to the put-call parity, which holds exactly in the Bates model, we focus on the pricing of call options.

To facilitate a comparison of the pricing errors for options with different moneyness and maturities, we map option prices to the Black-Scholes implied volatility (BSIV). Moreover, following Andersen, Fusari, and Todorov (2017), we define a normalized moneyness measure m_t as

$$m_t = \frac{\ln\left(\frac{K}{F_{t,T}}\right)}{\sqrt{T-t}\sigma_{atm}}, \tag{14}$$

where $F_{t,T}$ is the forward price of the stock for the same maturity as that of the option, while σ_{atm} is a constant volatility measure, which we set to be the average BSIV of at-the-money options from the entire sample.

When mapping the Bates model into the deep surrogate framework, there are 5 state variables, $s_t = [m_t, \tau, v_t, r_t, d_t]$, where $\tau = T - t$ is the time-to-maturity, and the instantaneous

[9] We apply the option pricing library QuantLib (https://www.quantlib.org) to compute prices and the corresponding BSIV.

variance v_t is latent. The risk-free rate r_t and dividend yield d_t are treated as observable states; they are assumed to remain constant over the life of the option but are allowed to vary with the time-to-maturity. In addition, there are 8 parameters, $\theta = [\kappa, \bar{v}, \sigma, \rho, \lambda, \nu_u, \nu_d, p]$. Thus, the dimension of the augmented state is $d = 13$.

3.2 Building the Deep Surrogate

The Bates model specified above belongs to the class of affine option pricing models, where the process of the underlying asset is an affine jump-diffusion under the risk-neutral measure. Berner, Grohs, and Jentzen (2020) (Theorem 1.1) show that, when approximating the solution in such models with a deep neural network, both the number of trainable network parameters and the size of the training sample grow only polynomially in the dimension of the input d.[10]

To construct the deep surrogate for the Bates model, we need to choose the activation function and the network architecture. Intuitively, the ReLU function appears to be a good candidate because of its resemblance to the option payoff in (13). However, we choose to use the *Swish* activation function (Ramachandran, Zoph, and Le, 2017),[11] which is given by

$$\sigma(x) = \frac{x}{1 + \exp(-\gamma x)}, \tag{15}$$

where γ can be a constant or a trainable parameter. The *Swish* activation function can be viewed as a smooth version of the ReLU function, and possesses two particular qualities that make it appropriate for the surrogate application: 1) unlike the *sigmoid*, it does not suffer from the vanishing gradient problem and, as our application shows, complex structural models require surrogate networks with a deep architecture, and 2) unlike *ReLU*, the *Swish* is smooth, which means that the gradients of the trained surrogate model will also be smooth across the state-space. This latter property is desirable when the gradients of the surrogate are needed (e.g., for estimation).

To illustrate this point, we train two surrogates, one with *Swish* and the other one with

[10] Berner, Grohs, and Jentzen (2020) consider affine diffusions, but their results can be readily extended to the type of jump-diffusion we consider. Their results are based on using ℓ_2-norm for the loss function. We use ℓ_1-norm for the loss function to reduce the influence of the outliers.

[11] It has been shown empirically that the performance of very deep neural nets in combination with *Swish* activation functions outperform architectures that rely on ReLU (see, e.g., Tripathy and Bilionis (2018)).

ReLU. Apart from the difference in activation function, the two surrogates are exactly alike: similar architecture, training procedure, training, and testing sample. We show that while the magnitudes of pricing errors of the *ReLU* and *Swish*-based surrogates are comparable, the approximation errors of option Deltas in the *ReLU* surrogate are substantially higher than those in the *Swish*-based surrogate. The details of these results are in Appendix D.

Next, we go over the details for generating the training sample, network architecture design, and the surrogate training procedure we use for the option pricing models.

Training sample and DNN architecture. To generate the training sample, we first obtain random draws $\tilde{x}_i$ from the input space $\mathcal{X}$. To do so, we set the minimum and maximum values for each state variable and all parameters (see Table A.1 in Appendix A), where the values for these upper and lower bounds are chosen based on a combination of model restrictions and domain knowledge. For example, the intensity of the Poisson process λ in the Bates model is, by definition, positive; the correlation between volatility shocks and price shocks ρ is restricted to be negative based on the so-called leverage effect documented in the literature.

We build the training samples and surrogate model following an iterative process described in Section 2.1, starting with a network of 3 layers and an initial training sample of 10^7 observations, then gradually increasing the training sample size and depth of the deep surrogate until the criterion (7) is met (a new validation set of size 10^6 is used in each iteration). At each step of network training, we run a mini-batch stochastic gradient descent algorithm to determine the neural network's parameters.[12] With this procedure, we obtain a final training sample of size 10^9. The final feedforward network for the Bates model for instance has 7 hidden layers, 400 neurons each. This architecture yields a total of 967,201 trainable parameters.

Although the final size of our training sample might appear large, it only sparsely populates the 13-dimensional augmented state space. It is also worth noting that we build the training sample using a naive scheme by randomly drawing points from the augmented state space

[12]Specifically, we run the ADAM optimization algorithm with an initial learning rate of $0.5 * 10^{-4}$ for 15 epochs, that is, we use mini-batches of size 256 until we have used the whole data set 15 times. After each epoch, we save the model and use a validation set of 10,000 points to estimate the surrogate model's performance. In the end, we use the network's parameters after the epoch with the lowest validation error.

Table 2: **Performance Improvement from Deep Surrogates**

This table compares the estimated computing time for pricing or getting the gradient of all the SPX options on an average day and daily estimation over a year using a traditional method based on Fast Fourier Transform (FFT) versus a Deep Surrogate model. We use the Bates model for illustration. We estimate the gradient of the FFT method through numerical differentiation, while the gradient of the Deep Surrogate can be obtained directly through backward propagation. To transform the daily gradient estimation into a yearly estimation of the model's parameters, we assume an average of 10 iterations of the optimization algorithm and 252 business days in a year.

	FFT	Deep Surrogate	Deep Surrogate + GPU
pricing, 1-day	10s	0.6s	0.06s
gradient, 1-day	180s	3.2s	0.3s
estimation, 1-year	125h	2.2h	0.2h

based on the uniform distribution. An active learning scheme (see, e.g. Krause and Guestrin, 2007; Deisenroth, Rasmussen, and Peters, 2009; Renner and Scheidegger, 2018), that is, one that samples more intensively in regions where nonlinearity is more pronounced and where initial approximation errors are large) is likely to be much more efficient.

Surrogate performance. To illustrate the magnitude of gains in computing speed, we compare the approximate computing time needed for pricing 4,000 European options (which is roughly the daily number of SPX options traded on the CBOE) with the Bates model based on three methods: direct evaluation of the pricing formula using the Fast Fourier Transform (FFT), deep surrogate using a single CPU, and deep surrogate using a GPU. We also compare the computing time for estimating the model parameters from option prices on a single day (assuming 10 iterations are needed in the parameter search), as well as the time required to perform daily estimation for an entire year. The results are shown in Table 2. Although the estimates can vary depending on hardware and implementation, the advantage of the deep surrogate relative to ordinary FFT, which suffers from the curse of dimensionality, is evident, especially when we take advantage of its parallelizability on a GPU.

A small validated pricing error is a necessary but not sufficient condition to consider a DNN accurate enough to be used as a surrogate for the option pricing model. It does not imply that it can approximate the function gradients (the option "greeks") accurately, nor

does it ensure that the surrogate can be used to accurately estimate model parameters. We verify these properties systematically in Section 3.3.

3.3 Accuracy of the Deep Surrogate

A main objective of our deep surrogate approach is to provide high-precision approximation to the solutions of high-dimensional models. The level of accuracy is critical for certain applications, such as in derivative pricing or parameter estimation. As discussed in Section 2.2, this accuracy is built on sound theoretical foundations. In this section, we examine the accuracy of the deep surrogate model in pricing and parameter estimation.

Pricing and Option Delta

First, we use the following procedure to examine how closely the deep surrogate can match the option prices and Deltas in the theoretical (Bates) model.

1. We divide options into 12 bins based on maturity and moneyness, with four categories for days-to-maturity τ ($1 < \tau \leqslant 7$, $7 < \tau \leqslant 30$, $30 < \tau \leqslant 90$, and $90 < \tau \leqslant 365$) and three for normalized moneyness m ($-9 \leqslant m \leqslant -1.8816$, $-1.8816 < m \leqslant -0.2381$, and $-0.2381 < m \leqslant 5$), where m is defined in Eq. (14). The cutoffs for m are based on the 33th and 66th percentile of the empirical distribution for m in the SPX option sample.

2. Within each maturity-moneyness bin, we randomly draw 20,000 call options. For each option, m_t and τ are drawn uniformly from their respective ranges in that bin; the rest of the states (v_t, r_t, d_t) and all the parameters $\theta = [\kappa, \bar{v}, \sigma, \rho, \lambda, \nu_u, \nu_d, p]$ are drawn uniformly from the range $[\underline{x} + \Delta, \overline{x} - \Delta]$, where $\underline{x}$ and $\overline{x}$ are given in Table A.1 in the Appendix of the paper, with $\Delta = 0.05 \cdot |\overline{x} - \underline{x}|$. The introduction of a small Δ ensures that we do not draw parameter values from regions too close to the boundary of the state space on which the surrogate is trained, where the accuracy of the surrogate will inevitably deteriorate.[13]

[13] Depending on the application, one can either enlarge the state space or sample more near the boundary of the given state space to improve the accuracy of the surrogate in these regions.

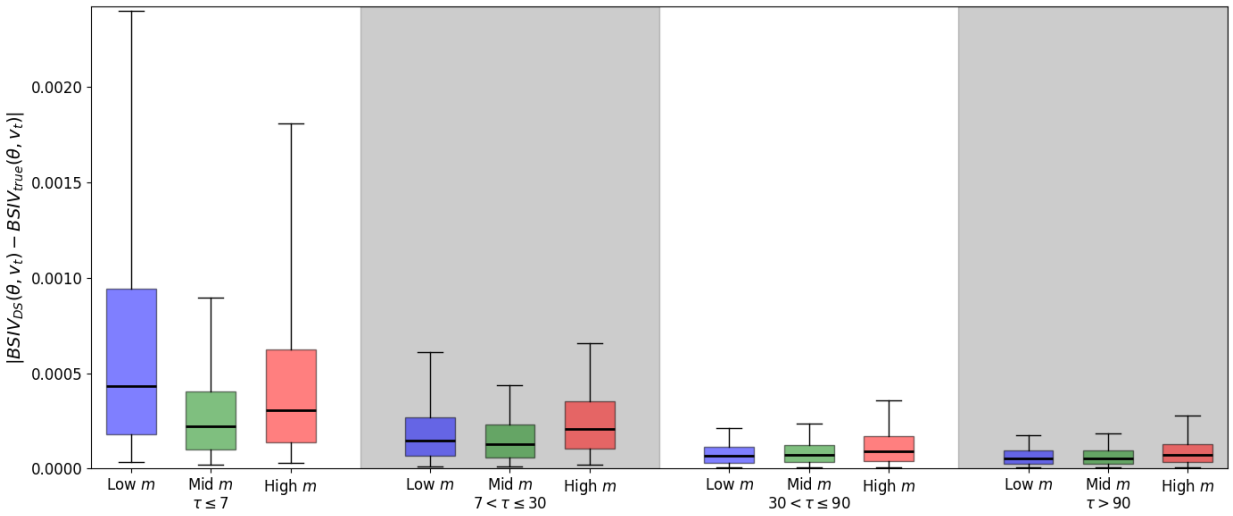

Figure 1: **Approximation Accuracy for the Deep Surrogate: BSIV.** This figure presents the distribution of the numerical mean absolute error (MAE) of the Bates surrogate. First, we generate 20,000 options with random parameters and states. For each option, we compute the Black-Scholes BSIV error by subtracting the surrogate-estimated BSIV from that of the "true" Bates model. We group these options into terciles based on their liquidity parameter m_i and time to maturity τ_i. Each box indicates the interquartile range, and the whiskers represent the MAE's 5th and 95th percentile.

3. We then price each option in two different ways, first based on the standard numerical solution of the Bates model (via Fast Fourier Transform as implemented by QuantLib), and then using the deep surrogate we built. The dollar prices obtained by these two methods are converted into BSIV, denoted by $BSIV_{true}$ and $BSIV_{DS}$, respectively. The absolute pricing error is given by $|BSIV_{DS} - BSIV_{true}|$.

Figure 1 shows the distributions of absolute pricing errors within each bin are summarized by boxplots. Figure 2 shows the distribution of absolute errors of options Deltas. The errors for pricing and option Delta generated by our trained deep surrogate relative to the target model are consistently small, especially when the time-to-maturity exceeds 7 days, where the 95th percentiles of the absolute pricing errors and Delta errors are both consistently below 0.0008. These errors are orders of magnitude smaller than the average BSIV and average Delta for the 12 bins, which are reported in Appendix A, Table A.2. In the cross-section, the deep surrogate appears to generate larger errors for those options with less than 7 days to maturity. However, even in those bins, the 95th percentile of absolute pricing errors is still less than 0.0025 (about 0.37% of the average for $BSIV_{true}$), and the 95th percentile of

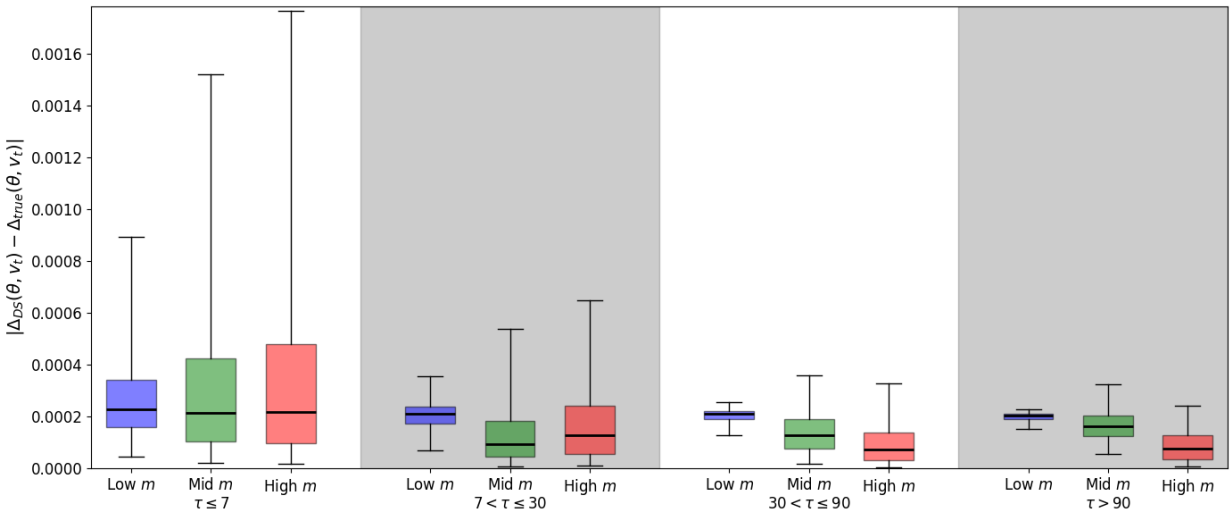

Figure 2: **Approximation Accuracy for the Deep Surrogate: Option Delta.** This figure presents the distribution of the numerical mean absolute error (MAE) of the Bates surrogate. For each box in this boxplot, we generate 20,000 options with random parameters and states. For each option, we compute Delta error by subtracting the surrogate-estimated Delta from that of the "true" Bates model estimated with Fast Fourier Transform. We group these options into terciles based on their liquidity parameter m_i and time to maturity τ_i. Each box indicates the interquartile range, and the whiskers represent MAE's 5th and 95th percentile.

absolute error for Delta is less than 0.0018 (about 0.87% of the average for Δ_{true}).

Parameter estimation errors

The previous experiment demonstrates that the surrogate produces an extremely low pricing and option Delta error when the parameters and hidden state are known. In reality, of course, those parameters have to be estimated *with* the surrogate model. Hence, our next numerical experiment uses the following procedure to assess the economic magnitude (in terms of out-of-sample pricing errors) of the parameter estimation errors with the deep surrogate.

1. We first draw the parameter vector $\theta = [\kappa, \bar{v}, \sigma, \rho, \lambda, \nu_u, \nu_d, p]$ and the rest of the states (v_t, r_t, d_t) uniformly from the range $[\underline{x} + \Delta, \overline{x} - \Delta]$ (see Table A.1, in Appendix A).[14]

2. We simulate a cross-section of 1,000 call options by randomly drawing their normalized

[14]As with previous experiment, by setting by setting $\Delta = 0.05 \cdot |\overline{x} - \underline{x}|$, we slightly reduce the range of the parameter values drawn to ensure that they are not too close to the boundary of the state space over which the surrogate is trained.

moneyness m and days-to-maturity τ from a uniform distribution between -9 and 5 (m) and between 2 and 365 (τ), and compute their prices using the standard numerical solution (via Fast Fourier Transform) based on the true parameter values and states drawn in Step 1.

3. We then use GMM and the deep surrogate to estimate θ and the hidden state v_t. The GMM estimates are denoted by $\hat{\theta}^{DS}$ and $\hat{v}_t^{DS}$. The observable states r_t and d_t are treated as known.

4. Next, we draw 20 new options from each of the 12 maturity-moneyness bins and compute the true BSIVs for this new set of options using the standard numerical solution under the true values of parameters θ and hidden state v_t, which we denote as $BSIV_{true}(\theta)$. These newly drawn options form our test set.

5. We compute the out-of-sample BSIVs using the standard numerical solution, but with the estimated $\hat{\theta}^{DS}$ and $\hat{v}_t^{DS}$ replacing the true values. We denote the result as $BSIV_{true}(\hat{\theta}^{DS}, \hat{v}_t^{DS})$. We then compute the out-of-sample absolute pricing error as $|BSIV_{true}(\hat{\theta}^{DS}, \hat{v}_t^{DS}) - BSIV_{true}(\theta, v_t)|$.

6. Steps 1 through 5 are repeated for 1,000 times. In total, we have 20,000 out-of-sample option prices for each maturity-moneyness bin. The distributions of the absolute pricing errors are summarized by boxplots.

Figure 3 shows the results. Unlike in Figure 1, where the pricing error $|BSIV_{DS}(\theta, v_t) - BSIV_{true}(\theta, v_t)|$ highlights the approximation errors of the deep surrogate relative to the FFT-based numerical solution (with both solutions computed under the true parameter values θ and hidden state v_t), the pricing error in Figure 3, $|BSIV_{true}(\hat{\theta}^{DS}, \hat{v}_t^{DS}) - BSIV_{true}(\theta, v_t)|$, isolates the impact of parameter estimation errors on option pricing by computing both solutions with the same numerical solution.[15]

[15]We also report results on the magnitude of parameter estimation errors in Figure A.2 in Appendix B. Notice that the approximation errors of the deep surrogate act as a form of non-local model misspecification, which can magnify the estimation errors for those weakly identified parameters (those that option prices show low sensitivity towards). At the same time, the low sensitivity also means that the impact of their estimation errors on option prices will be small.

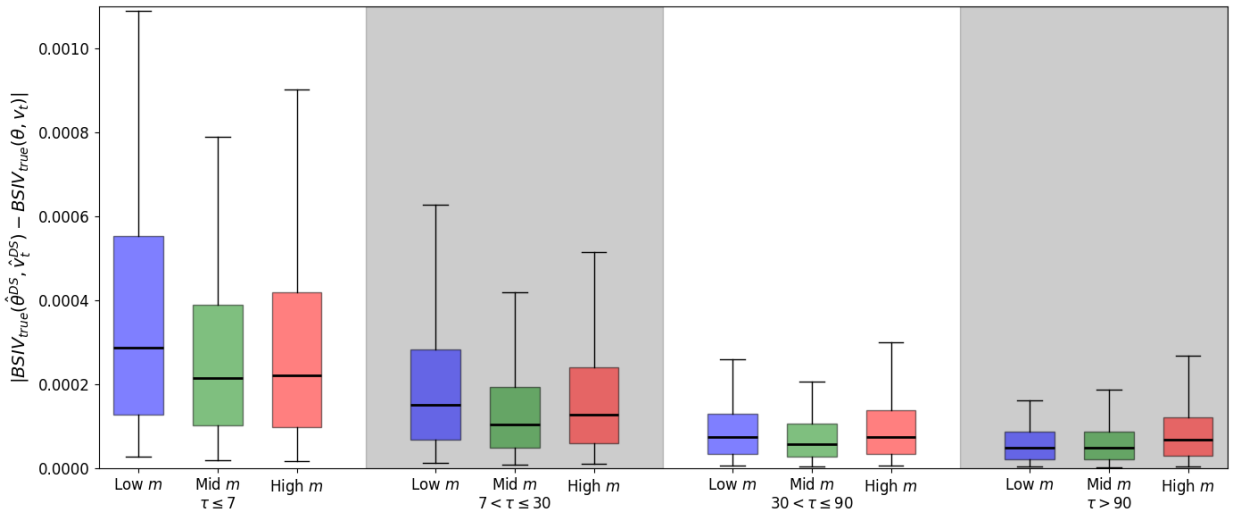

Figure 3: **OOS pricing errors due to parameter estimation errors.** This figure shows the distribution of the out-of-sample pricing errors resulting from the estimation errors caused by the deep surrogate. Each box indicates the interquartile range of the pricing errors for a given maturity-moneyness bin, and the whiskers represent the 5th and 95th percentile estimation errors across the simulations.

These pricing errors are consistently small across different maturity and moneyness bins. Indeed, they are orders of magnitude smaller than the average BSIV for the respective maturity-moneyness bins (see Table A.2 in Appendix A). As in Figure 1, the errors are larger for shorter maturity options. This is not a coincidence. Because the deep surrogate is less accurate when pricing short-dated options, it also results in parameter estimation errors in the directions that affect the pricing of short-dated options more.

4 Empirical Analysis

In this section, we apply the deep surrogate to study the structural option pricing model introduced in Section 3.1 in real data. With the help of the deep surrogate, we conduct daily re-estimation of the model parameters. This allows us to i) construct a high-frequency option-implied tail risk index for the stock market, ii) quantify the time variation in the degree of parameter instability and study its implications for option market liquidity, and iii) systematically examine the out-of-sample performances of the Bates model. Finally, we use the surrogate to characterize the model-implied conditional distributions of option returns

and confront them with the data.

We use daily data for the S&P500 index options (SPX) from OptionMetrics. Our sample includes European call and put options between 1996 and 2019. We apply standard filters (see, e.g., Andersen, Fusari, and Todorov, 2015) and discard all in-the-money options, as well as highly illiquid options with a bid-ask spread above 0.5. Finally, we filter on maturity and moneyness by keeping only options that satisfy: $1 \leqslant \tau_{i,t} \leqslant 365$ and $-9 \leqslant m_{i,t} \leqslant 5$. These last two filters ensure that the options in our sample fall within our surrogate training range (see Table A.1). Figure A.4 in Appendix C provides a summary of our sample.

We also obtain the zero-coupon yield curves as well as the forward prices of different maturities for the S&P 500 index from OptionMetrics. In addition, we obtain LTP (left-tail probability), an option-based estimate of the (risk-neutral) probability of a 10% weekly down move for the S&P 500 index, from Bollerslev, Todorov, and Xu (2015) and the VIX volatility index from the CBOE.

4.1 Tail Risk Index

On day t, for each option contract i, we calculate the maturity-specific risk-free rate r_{it} by interpolating the zero-coupon yield curve for that day. In addition, we calculate the maturity-specific dividend yield d_{it} based on the forward price of the same maturity ($F_{t,T}$) using the formula

$$d_{it} = r_{it} - \ln\left(\frac{F_{t,T}}{S_t}\right) / \left(\frac{\tau_{it}}{252}\right). \tag{16}$$

We then estimate the latent state v_t and model paramters $\theta = [\kappa, \bar{v}, \sigma, \rho, \lambda, \nu_u, \nu_d, p]$ for day t by fitting the BSIVs of the cross-section of SPX options using GMM with an identity weighting matrix (see (8)). As Table 2 suggests, this task would have been prohibitively expensive in terms of computing time, but becomes feasible on a normal computer thanks to the deep surrogate.

In Figure 4, we plot the smoothed time series for the latent state v_t and the parameters based on moving averages over the past 60 days. Strikingly, all of the parameter estimates show substantial time variation, which conveys unique information from the options market.

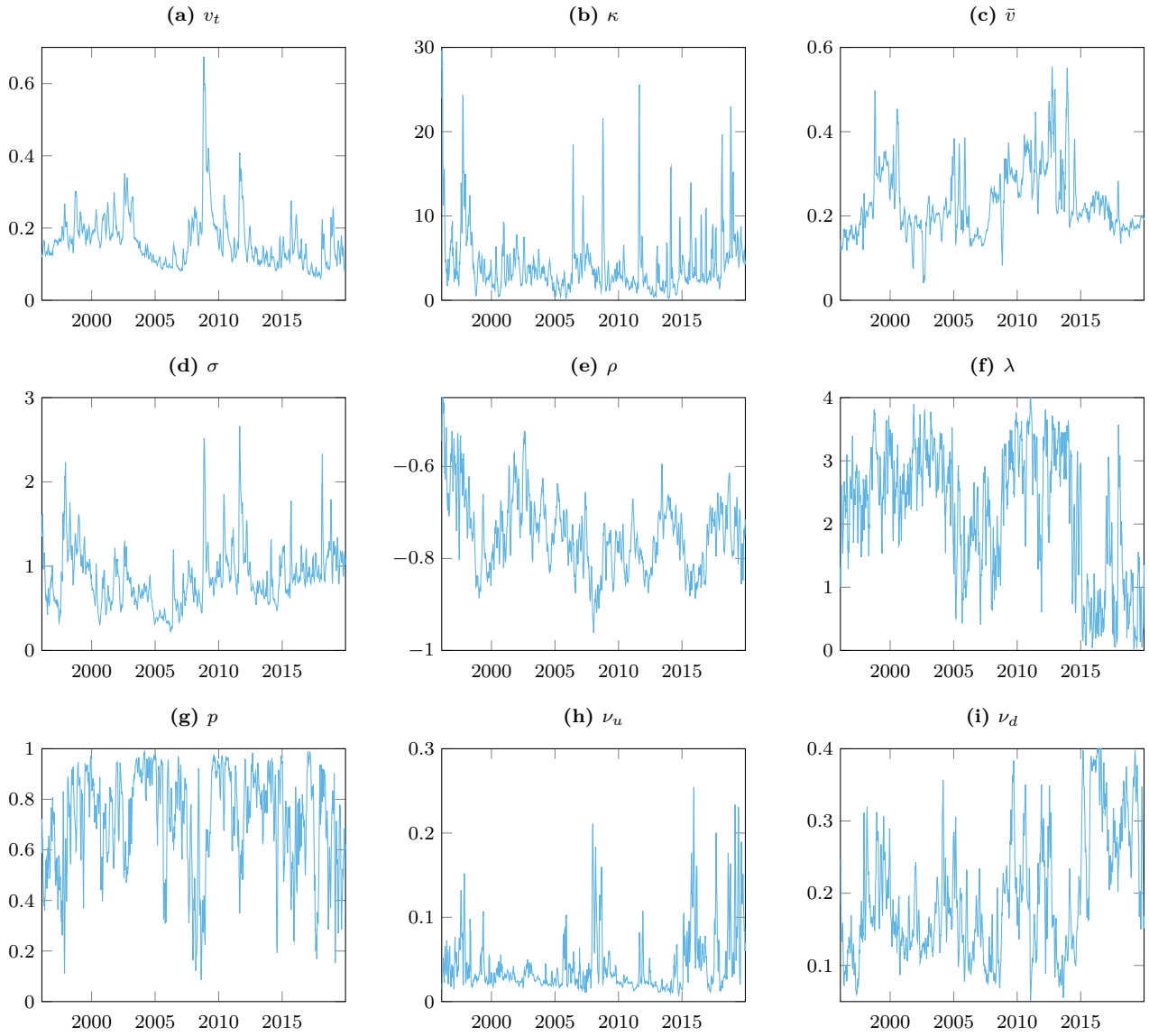

Figure 4: **Parameter estimates for the Bates model.** This figure shows the smoothed (20-day rolling means) daily estimates of the parameters and latent state of the Bates model.

For example, the parameter ρ, which is the conditional correlation between shocks to stock price S_t and instantaneous variance v_t, provides an option-based measure of the so-called leverage effect (see e.g., Black, 1976). It ranges between -0.5 to -0.9 in most of our sample, and noticeably turned most negative during the Great Financial Crisis, reaching -0.96 in early 2008. As another example, the options market provides clear evidence that asymmetry between upward and downward jumps in the market index is needed to fit the option prices; we can see it through the fluctuations in p, the conditional probability of an upward jump, as well as ν_u and ν_d, which measure the expected size of upward and downward jumps.

Predicting tail events. We now focus specifically on the information that the option market conveys about tail risk in the market index. We define two measures of left-tail risks based on the parameter estimates on date t,

$$TailProb_t = \lambda_t \frac{n}{252}(1-p_t)e^{-\frac{\alpha}{\nu_{d,t}}}, \tag{17a}$$

$$TailRisk_t = \lambda_t \frac{n}{252}(1-p_t)\left(1-\frac{1}{1+\nu_{d,t}}\right). \tag{17b}$$

The first measure, $TailProb_t$, is approximately the risk-neutral probability of a negative jump of size α in the S&P 500 index over the next n days, which assumes that the parameter values will remain the same in the next n days and ignores the probability of more than one jumps. The second measure, $TailRisk_t$, is approximately the risk-neutral expected loss in the index due to a negative jump over the next n days, again ignoring the probability of more than one jump.

In Panel A of Figure 5, we compare $TailProb$ with $n = 5$ and $\alpha = 10\%$ against Left Tail Probability (LTP) estimator from Bollerslev, Todorov, and Xu (2015), which is also a measure of the risk-neutral probability of a 10% down move for the S&P 500 index over a week. The measure LTP is based on a nonparametric model and is estimated exclusively with short-dated (with a tenor between 6 and 31 trading days) deep out-of-the-money SPX options. Interestingly, despite the differences in methodology, the two series show similar magnitudes overall and have a correlation of 0.71 in our sample; LTP has more pronounced peaks compared to $TailProb_t$, especially before 2013. In Panel B, we plot the tail risk index $TailRisk_t$, which is also highly correlated with LTP and even more so with $TailProb$.

To discern the differences in their information content, we use the three tail risk measures to predict the probability of a left-tail event in the S&P 500 index over the next h periods, $P_t(TailEvent_{t+h})$, through a logistic regression:

$$P_t(TailEvent_{t+h}) = \frac{1}{1+\exp(-\beta_0 - \beta_1\, LTP_t - \beta_2\, TailProb_t - \beta_3\, TailRisk_t)}. \tag{18}$$

In order to have a reasonable number of tail events in our sample, we define a tail event in two different ways: i) a cumulative return of -10% or less in the index over the next 5

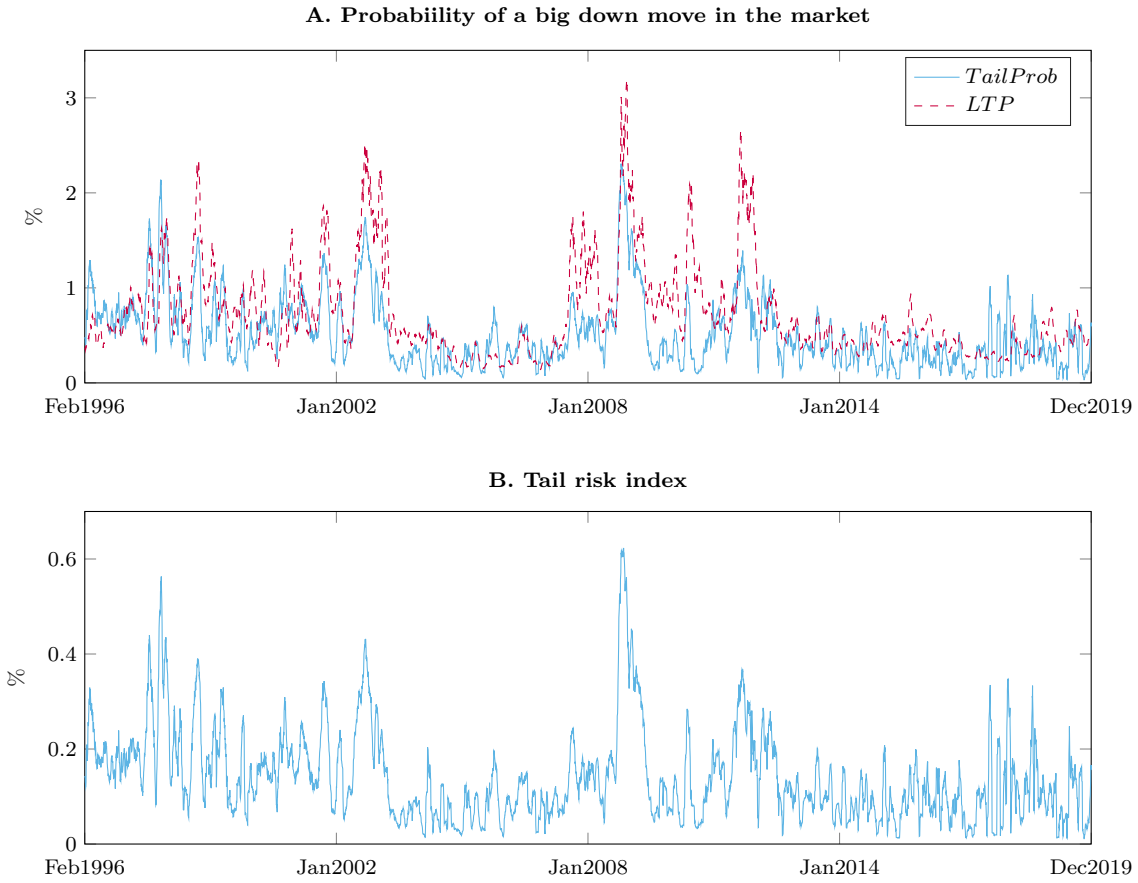

Figure 5: **Option-implied tail risk measures.** In Panel A, we compare the risk-neutral probability of a 10% negative jump in the S&P 500 index over the next 5 days based on $TailProb$ from the Bates model against that by LTP from Bollerslev, Todorov, and Xu (2015). In Panel B, we plot $TailRisk$, the risk-neutral expected loss in the S&P 500 index resulting from a negative jump over the next 5 days. Both $TailProb$ and $TailRisk$ are based on 20-day rolling means.

business days; ii) a daily return of -5% or less for any individual days over the next 5 business days. We define $TailProb$ accordingly, with $n = 5$ and $\alpha = 5\%$.

As Table 3 shows, individually, the three tail risk measures can all predict the two types of tail events we consider, with coefficients that are highly statistically significant. The economic magnitude is also significant. For example, a one-standard-deviation increase in $TailProb$ is associated with approximately an 80% (relative) increase in the probability of a 5% daily drop of the index in the next week; with a one-standard-deviation increase in $TailRisk$, the probability of the same event nearly triples. The pseudo-R^2 coefficient is the highest with $TailRisk$ as the predictor. When predicting 5% daily drops, the pseudo-R^2

Table 3: **Predicting Tail Events**

This table presents the results of the logistic regression used to predict jumps in the S&P 500. $TailEvent_{t+h}$ is defined in two different ways. In Panel A, a tail event is defined as a cumulative return of -10% or less over the next 5 business days. In Panel B, a tail event is defined as a daily return of -5% or less for any individual days over the next 5 business days. The values in parentheses are heteroskedasticity and autocorrelation consistent (HAC) standard errors (with 13 lags); * denotes significance at the 10% level, ** at 5%, and *** at 1%. The sample period is from January 1996 to December 2019, with 5,939 observations. The adjusted McFadden Pseudo-R^2 coefficients are included.

	10% Weekly Down Move				5% Daily Drop within a Week			
	(1)	(2)	(3)	(4)	(5)	(6)	(7)	(8)
LTP	1.468***			0.052	1.917***			-0.364
	(0.365)			(0.777)	(0.423)			(0.694)
$TailProb$		1.258***		-0.935		1.601***		-3.272***
		(0.188)		(0.812)		(0.218)		(0.716)
$TailRisk$			8.131***	12.917**			11.177***	29.903***
			(1.027)	(5.643)			(1.263)	(5.453)
Constant	-7.190***	-6.776***	-6.907***	-6.854***	-6.569***	-5.980***	-6.383***	-5.992***
	(0.606)	(0.405)	(0.407)	(0.599)	(0.677)	(0.410)	(0.461)	(0.539)
Pseudo-R^2	0.080	0.119	0.152	0.159	0.173	0.230	0.331	0.386

nearly doubles, rising from 17.3% with LTP to 33.1% with $TailRisk$. When we use the three predictors jointly, the coefficient for LTP is no longer significant but remains significant for $TailRisk$, while the adjusted pseudo-R^2 only rises marginally compared to the case with having $TailRisk$ as the only predictor, suggesting again that much of the predictive information for future tail events is contained in the measure $TailRisk$.

4.2 Parameter Instability

If a structural model is correctly specified, we should expect to see its parameter estimates from sub-samples remain stable. However, Figure 4 shows that the parameter estimates for the Bates model fluctuate significantly over time. For some of the parameters (e.g., $\bar{v}$ and σ), the dynamics appear to be relatively persistent, which means that one can address the issue by re-calibrating the parameters frequently to adapt to the latest data. However, for other parameters, such as λ and p, the estimated parameter values can change drastically in a short period of time. Such type of parameter instabilities cast doubt about how reliable a model fitted with the historical data will be out of sample, which in turn has implications for

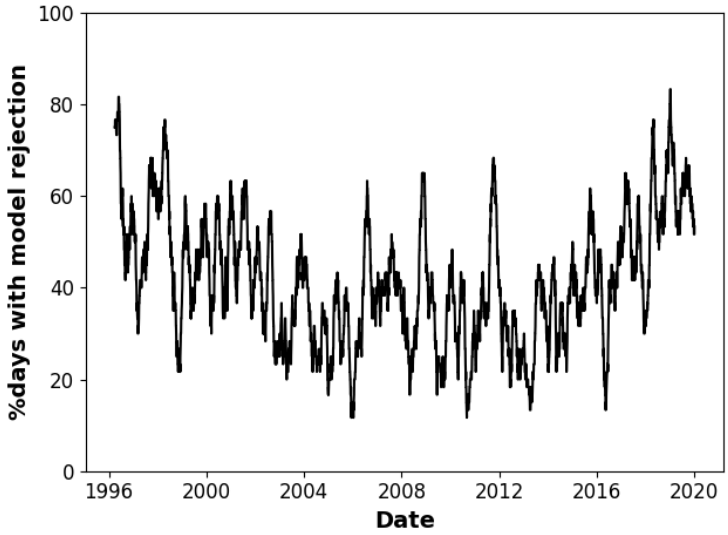

Figure 6: **Rejection rates for parameter stability tests.** This figure shows, for each day, the percentage of the last 60 days for which the parameter estimates of the Bates model are statistically significantly different (at the 1% level) on two adjacent trading days.

options trading and risk management.

In this section, we formally test whether the Bates model parameters are stable at a daily frequency. The reason for choosing the daily frequency is to inform us whether daily model recalibration could be sufficient to address the parameter instability issue. Performing the tests at lower frequencies (say monthly or annually), although less demanding computationally, is incapable of revealing the problem at higher frequencies.

We apply the statistical test developed by Andersen, Fusari, and Todorov (2015). Consider dates t and $t-1$. We define the parameter instability measure I_t on date t as

$$I_t \equiv \left(\hat{\theta}_t - \hat{\theta}_{t-1}\right)' \left(\widehat{\text{Avar}}\left(\hat{\theta}_t\right) + \widehat{\text{Avar}}\left(\hat{\theta}_{t-1}\right)\right)^{-1} \left(\hat{\theta}_t - \hat{\theta}_{t-1}\right), \tag{19}$$

where $\hat{\theta}_t$ denotes the parameter estimates on date t, and $\widehat{\text{Avar}}\left(\hat{\theta}_t\right)$ denotes consistent estimate of the asymptotic variance of $\hat{\theta}_t$ (cf. Andersen, Fusari, and Todorov (2015), equations (11)-(12)). Under the null hypothesis that the option pricing model is valid for the two distinct periods, I_t is asymptotically chi-squared distributed with degrees of freedom p. Thus, it is straightforward to test whether the GMM estimates $\hat{\theta}_{GMM,t}$ on each date t are statistically different from those on date $t-1$.

Figure 6 shows the results of the daily parameter stability tests for the Bates model. On the y-axis, we show the average percentage of days over the past 60 days for which the hypothesis was rejected at the 1% level. On average, we reject daily parameter stability at the 1% level 41.6% of the time, but the rejection rate fluctuates between 20 and 80% over the sample and shows some persistence. In comparison, the rejection rate for the Heston model (Heston, 1993), which features stochastic volatility but no jumps in the price dynamics of the underlying asset, is even higher, at 60.7% on average, an indication of more severe misspecification.[16]

A potential economic consequence of parameter instability is that it becomes more difficult to manage the risks of an option portfolio. An important method for option market makers to manage inventory risks is to Delta-hedge their inventory positions, where the hedge ratios are produced by some model. While market makers can use a variety of option pricing models, our parameter instability measure based on the Bates model can help identify periods of model instability more broadly, during which time the hedge ratios produced by a model that is calibrated to past data may not accurately predict future sensitivities of option values to changes in stock prices. This would elevate the risks of market making and reduce the liquidity in the market.

To examine this prediction, we run panel regressions of option bid-ask spreads on the parameter instability measure,

$$BidAsk_{i,t} = \alpha_i + \beta_1 \ln I_t + \beta_2 BidAsk_{i,t-1} + \beta_3 VIX_t + \beta_4 LTP_t + \beta_5' X_{i,t} + \epsilon_{i,t}. \tag{20}$$

Here, $BidAsk_{i,t}$ is the relative bid-ask spread for option i at time t, defined as the closing bid-ask spread normalized by the mid-quote. Besides the log of the parameter instability measure $\ln(I_t)$, we include the contract fixed effect α_i and lagged bid-ask spread as controls. For market conditions, we control for the market volatility index VIX_t, and the tail risk measure LTP_t. Finally, the contract-specific controls $X_{i,t}$ include option tenor, $\tau_{i,t}$, out-of-the money binary variable equal to 1 if $|m_{i,t}| > 1$ ($OTM_{i,t}$), and abnormal volume, $\widehat{Volume}_{i,t}$,

[16]The results for the deep surrogate for the Heston model, unreported here, are available upon request.

Table 4: **Parameter Instability and Option Bid-Ask Spreads**

This table presents the results of panel regressions of option bid-ask spreads on the parameter instability measure. The values in parentheses are heteroskedasticity consistent standard errors clustered by contract; * denotes significance at the 10% level, ** at 5%, and *** at 1%. The sample includes all SPX options from January 1996 to December 2019, with 5,314,757 contract-day observations.

	(1)	(2)	(3)	(4)
$ln(I_t)$	-0.013***	0.0286***	0.0279***	0.0243***
	(0.0015)	(0.0016)	(0.0016)	(0.0016)
$BidAsk_{i,t-1}$	0.766***	0.764***	0.7631***	0.6821***
	(0.0008)	(0.0008)	(0.0008)	(0.001)
VIX_t		-9.2132***	-9.3504***	-8.2397***
		(0.1879)	(0.1895)	(0.1978)
LTP_t		0.3197***	0.308***	0.1325***
		(0.0342)	(0.034)	(0.0315)
$\widehat{Volume}_{i,t}$			0.0081***	-0.0017***
			(0.0002)	(0.0002)
$\tau_{i,t}$				-0.0174***
				(0.0002)
$OTM_{i,t}$				3.6474***
				(0.0212)
Contract FE	Yes	Yes	Yes	Yes
R^2	0.765800	0.766200	0.766300	0.779000

which is defined as

$$\widehat{Volume}_{i,t} = \frac{Volume_{i,t}}{\frac{1}{252}\sum_{k=1}^{252} Volume_{i,t-k+1}} - 1, \tag{21}$$

where $Volume_{i,t}$ is the trading volume of contract i on date t.

The results are reported in Table 4. When we only control for lagged bid-ask spread and contract fixed effect, the coefficient on $ln(I_t)$ is negative. This is likely because the degree of parameter instability is positively correlated with market volatility and tail risk. SPX puts tend to be traded more actively when the market is volatile, which can reduce the bid-ask spreads. To isolate the effect of parameter instability from market volatility,

we include both VIX_t and LTP_t as controls, after which the coefficient on $ln(I_t)$ becomes significantly positive. Controlling for abnormal volume at the contract level has little effect on the coefficient for $ln(I_t)$. After further controlling for contract tenor and out-of-the-money indicator, both of which are related to option liquidity themselves (for example, long-dated options and deep OTM options tend to be less liquid), the coefficient for $ln(I_t)$ is smaller but remains highly significant. Overall, the results in Table 4 are consistent with the prediction that bid-ask spreads will widen when the option pricing models that market makers are using become more unstable.

4.3 Out-of-sample Performance

Besides risk management, parameter instability will also affect a structural model's out-of-sample performance. In this section, we examine the out-of-sample pricing and hedging performances of the Bates model based on daily re-estimation, and compare it to a non-parametric model.

To measure the out-of-sample pricing errors, we estimate the Bates model's parameters θ and hidden state v_t on date t, and then use them to predict the mid bid-ask BSIVs of all the out-of-money (OTM) SPX call and put options at time $t + h$ under the updated values for the observable states (including normalized moneyness m_{t+h}, time-to-maturity τ, risk-free rate r_{t+h}, and dividend yield d_{t+h}). For all of the results to follow, we set $h = 5$ to examine the performance one week ahead. For simplicity, we keep the latent state constant, $v_{t+h} = v_t$.

Reduced-form benchmark. Motivated by Christoffersen and Jacobs (2004), we use a reduced-form model as an evaluation benchmark for the Bates model. The comparison also helps shed light on the relative strengths and weaknesses of the structural option pricing model relative to reduced-form models, which are becoming increasingly popular with the advances in machine learning. Christoffersen and Jacobs (2004) consider a so-called Practitioner Black-Scholes model, which models the implied volatility surface using a polynomial of time-to-maturity and strike price. We extend this approach by replacing the polynomial with

a more flexible random forest (RF) model.[17]

The random forest model's input is

$$X_{i,t} = [m_{i,t}, \tau_{i,t}, m_{i,t}\tau_{i,t}, \mathbb{1}_{m_{i,t}}], \tag{22}$$

where m is the moneyness measure defined in (14), τ is the time-to-maturity, and $\mathbb{1}_m$ is a binary indicator that equals to 1 if $m_{i,t} > 0$ (the option's strike is above the corresponding forward price). Although a nonlinear model like the random forest should, in principle, be able to recover the two features $m_{i,t}\tau_{i,t}$ and $\mathbb{1}_{m,i,t}$ from $m_{i,t}$ and $\tau_{i,t}$, we include them to speed up the algorithm training. Consistent with the way we re-estimate the parameters of the Bates model at daily frequency, we also retrain the random forest model daily to minimize the mean squared error (MSE) of the BSIVs for all SPX options each day.

In Figure 7, we plot the average implied-volatility RMSEs of SPX options at different strikes (with the underlying index level normalized to 100) for the Bates model and the RF model. Since we only use OTM options from the data, the options in our sample with strike prices less (more) than 100 are puts (calls). Panel (a) shows the in-sample pricing performances for all maturities, while panels (b) through (d) report the out-of-sample performances at a weekly horizon ($h = 5$) for different maturity buckets.

As expected, the out-of-sample RMSEs are significantly higher than the in-sample RMSEs for both models. The RF model, in particular, is able to match the data closely in the sample thanks to its flexibility, with RMSEs less than 0.003. For reference, the average BSIV of all options in our sample is 0.218. For both models, the out-of-sample RMSEs are the highest for short-dated options and become smaller at longer maturities; they also tend to be higher for high strikes (deep out-of-the-money calls).

Interestingly, as Panel (a) of Figure 7 shows, the RF model produces substantially smaller out-of-sample pricing errors than the Bates model for the extremely short-dated options (with time-to-maturity of 7 days or less). The Bates model struggles the most in pricing short-dated deep OTM puts and OTM calls. For 20% OTM puts, the RMSEs for the Bates

[17] A random forest works by constructing a multitude of decision trees, with the algorithm's prediction defined as the mean output of each individual tree. This ensemble approach drastically reduces the risk of over-fitting. For a general introduction to random forests, see Liaw, Wiener et al. (2002), and for random forests applied to finance, see, e.g., Gu, Kelly, and Xiu (2018).

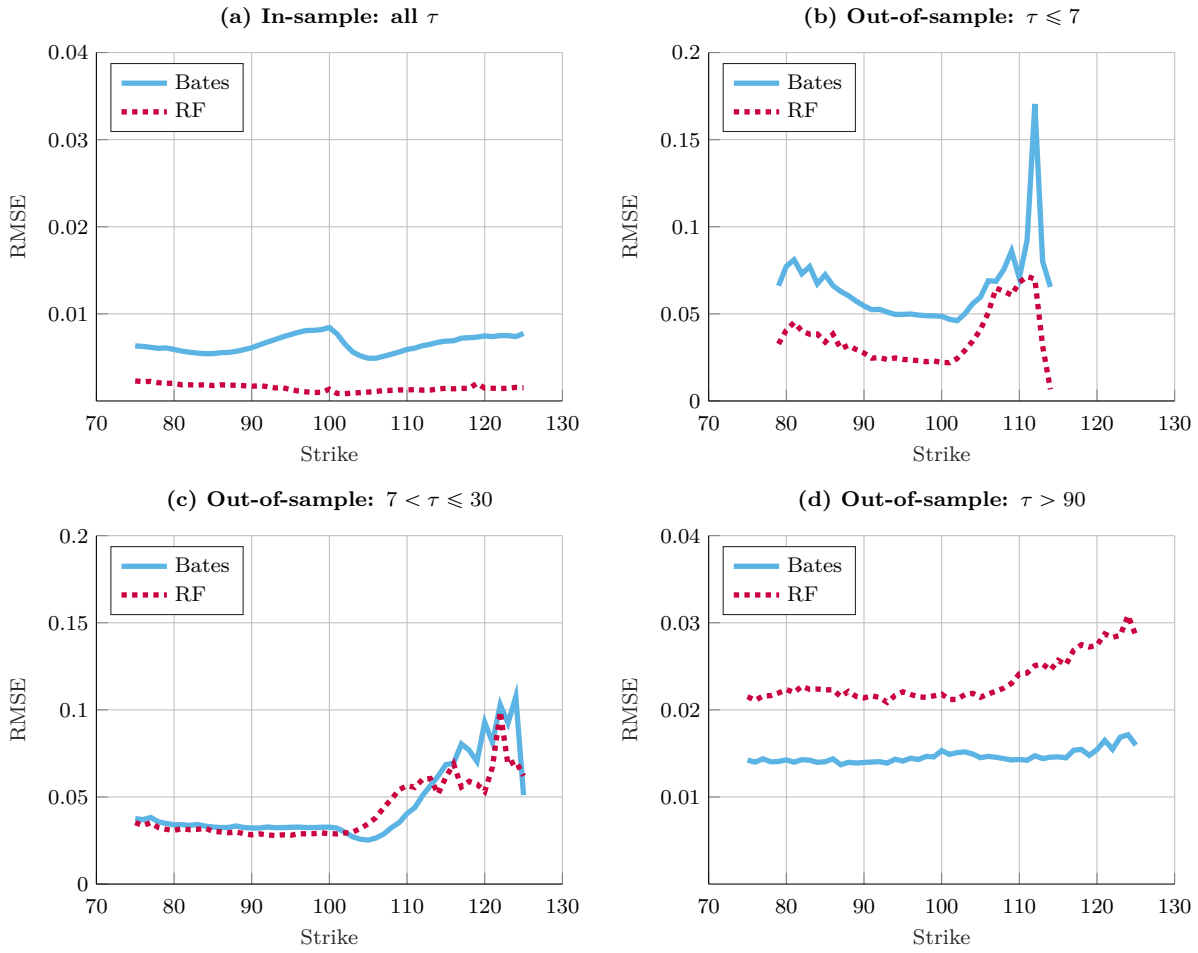

Figure 7: **Pricing performances of the Bates model and RF model across different strikes and tenors.** This figure shows the model's in- and out-of-sample performances, as measured by averages of daily RMSEs, across different strikes and maturity brackets. For out-of-sample performance, the forecasting horizon is one week ($h = 5$).

model are as high as 0.08, compared to 0.04 or lower for the RF model; for 10%+ OTM calls, the RMSEs for the Bates model are as high as 0.17, compared to 0.07 or lower for the RF model. However, the advantage of the RF model dissipates as we move to longer maturity. For options with time-to-maturity above 90 days, the Bates model actually outperforms the RF model, which is clearly demonstrated in Panel (d).

The dependence of the relative performances of the structural Bates model and the reduced-form RF model on time-to-maturity is a nice illustration of the bias-variance tradeoff. As Andersen, Fusari, and Todorov (2017) demonstrate, short-dated options are different from longer-dated options in terms of the type of risks they are most exposed to. For example, short-dated options are not as sensitive to changes in the expected volatility of the underlying

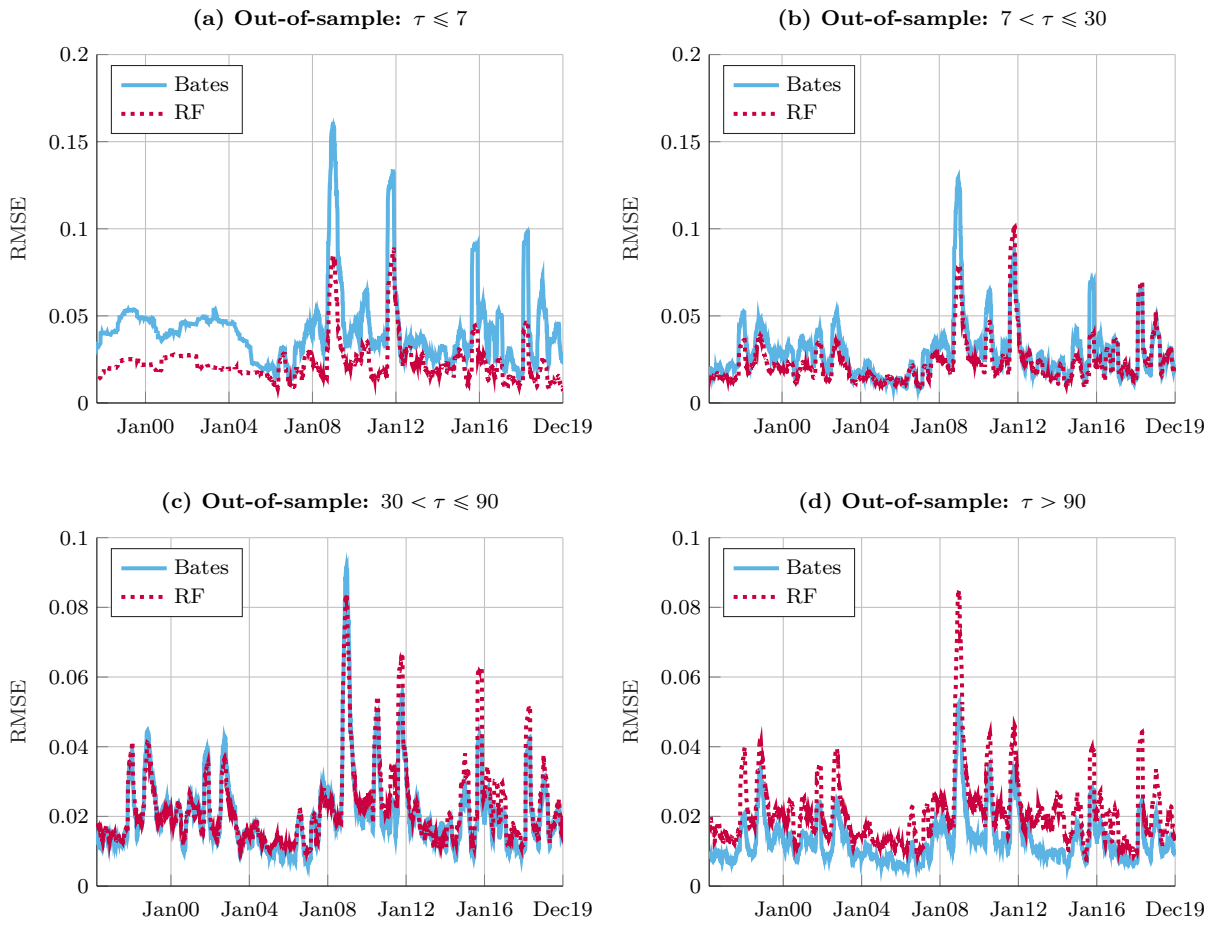

Figure 8: **Pricing performances of the Bates model and RF model over time.** This figure shows the model's out-of-sample performances, as measured by averages of daily RMSEs over 60 days, across maturity brackets. For out-of-sample performance, the forecasting horizon is one week ($h = 5$).

asset, but are highly sensitive to the level of spot volatility and jump intensity, as well as the distribution of the jump size. Additionally, short-dated options could also be more severely affected by liquidity and demand factors (due to investors rolling over their maturing positions as well as higher retail investor participation in the case of OTM calls). Our results on the relative performances suggest that the RF model benefits from its flexibility when pricing short-dated options, for which the Bates model is more severely misspecified; in contrast, the Bates model is better suited to capture the intertemporal changes in risks that matter more for longer-dated options, and its parsimony helps guard against over-fitting, which hurts the performance of the RF model. Our results provide systematic justification for the standard practice of filtering out extremely short-dated options in the literature.

Next, in Figure 8, we compare the out-of-sample pricing performances of the Bates model and the RF model over time. The four panels are for four different maturity buckets. Confirming the findings in Figure 7, the RF model consistently outperforms the Bates model for short-dated options (with $\tau \leqslant 7$) throughout our sample period, and the reverse is true for long-dated options (with $\tau > 90$). In the shortest maturity category (Panel (a)), the pricing errors become more volatile after the introduction of weekly SPX options in 2005, especially for the Bates model. Across maturities, the pricing errors spike up periodically, most notably in Q4 2008 (during the Great Financial Crisis), and also in Q4 2011, Q2-Q3 2015, and Q1 2018. As expected, the timings of the spikes in pricing errors for the Bates model correspond to periods of high parameter instability, as shown in Figure 6. However, the strong correlation between the pricing errors of the Bates model and the RF model is evidence that the time variation in parameter instability for the Bates model reflects a more general form of model instability.

Finally, we also compare the out-of-sample hedging performances for the Bates model against that for the RF model and the Black-Scholes (BS) model. We measure the hedging errors for contract i from date $t-1$ to t as

$$\epsilon_{i,t}^{(m)} = \frac{(p_{i,t} - p_{i,t-1}) - \Delta_{i,t-1}^{(m)}(S_t - S_{t-1})}{p_{t-1}}, \quad m \in \{\text{Bates}, \text{BS}, \text{RF}\}, \tag{23}$$

where $\Delta_{i,t-1}^{(m)}$ is the model-implied Delta from $t-1$, S_t is the closing price of the underlying asset at time t, and $p_{i,t}$ is the mid quote of option i at time t. We standardize the error by the option price at time $t-1$.

Among the three models, the RF model produces the highest mean absolute hedging error, likely because it is trained to match option prices but does not face any constraint on the Delta it produces. The Bates model consistently produces the smallest hedging errors, even for short-dated options, where they produce larger pricing errors. This finding echoes the finding of Schaefer and Strebulaev (2008) in the corporate bond market. It shows that structural models are informative about out-of-sample hedge ratios even though they might imply large pricing errors.

Structural vs. reduced-form model. The previous results suggest that the performance of the structural Bates model relative to that of the non-parametric Random Forest model changes in the cross section and over the time series. Figure 7 shows that the Bates model under-performs the RF model for shorter-dated options (with days-to-maturity of 7 days or less) across different moneyness but outperforms the latter for longer-dated options (with days-to-maturity longer than 90 days). In addition, Figure 8 shows that the OOS pricing errors of both models vary significantly over time.

To systematically analyze how the relative performance between the two models depends on contract characteristics and market conditions, we run the following panel regression,

$$\begin{aligned} AE_{i,t}^{Bates} - AE_{i,t}^{RF} = \alpha_i + \beta_1 VIX_t + \beta_2 \Delta VIX_t + \beta_3 LTP_t + \beta_4 \Delta LTP_t \\ + \beta_5 BidAsk_{i,t} + \beta_6 T_{i,t}^{1-7} + \beta_7 OTM_{i,t} + \beta_8 D_{i,t} + \epsilon_{i,t}. \end{aligned} \tag{24}$$

On the left-hand side of (24), $AE_{i,t}^{j}$ is the absolute pricing error (measured in terms of BSIV) that model j ($j \in \{Bates, RF\}$) produces for contract i on date t. On the ride-hand side, α_i is the contract fixed effect. There are four market-level controls. VIX_t is the level of the VIX index on date t, while ΔVIX_t is the difference in VIX between date t, when the performance is measured, and $t-5$, when the model is calibrated, i.e., $\Delta VIX_t = \frac{VIX_t}{VIX_{t-5}} - 1$. Similarly, LTP_t is the left-tail jump probability measure of Bollerslev, Todorov, and Xu (2015) on date t, and $\Delta LTP_t = \frac{LTP_t}{LTP_{t-5}} - 1$. These controls allow us to examine how different market conditions affect the relative performances of the two models.

We also have four contract-day level controls. $BidAsk_{i,t}$ is the relative bid-ask spread for option contract i on date t, which is a proxy for the liquidity of the option. $T_{i,t}^{1-7}$ is a dummy variable that equals 1 if the option's time-to-maturity is 7 days or less. $OTM_{i,t}$ is an indicator for calls and puts that are sufficiently deep OTM (recall that we have excluded all ITM options from the sample). It is equal to 1 if $|m_{i,t}| > 1$ and 0 otherwise. $D_{i,t}$ is the Mahalanobis distance between the input features for contract i on date t and the distribution of contract features of all the options in the training sample used to calibrate the model at

time $t-5$. Specifically,

$$D_{i,t} = \sqrt{(\mathbf{x}_{i,t} - \boldsymbol{\mu}_{i,t-5})^T \mathbf{S}_{i,t-5}^{-1} (\mathbf{x} - \boldsymbol{\mu}_{i,t-5})}, \tag{25}$$

where $\mathbf{x}_{i,t} = [K_{i,t}, \tau_{i,t}]$ is a vector containing the strike and time-to-maturity of an individual option. $\boldsymbol{\mu}_{i,t-5} = \frac{1}{N_{t-5}} \sum_{i}^{N_{t-5}} \mathbf{x}_{i,t-5}$ is the mean of all the vector $\mathbf{x}_{i,t}$ used to calibrate the model at time $t-5$. $\mathbf{S}_{i,t-5}^{-1}$ is the inverse of the covariance matrix of the vectors $\mathbf{x}_{i,t-5}$. Intuitively, a higher value for $D_{i,t}$ indicates that the contract appears more different from the mass of the contracts in the training sample based on its strike and maturity.

Table 5 presents the results.[18] A negative coefficient for a covariate implies that the Bates model's accuracy improves relative to the RF when the value of that covariate rises. In the setting with the complete set of controls (Specification (6)), the coefficient estimates for the levels of VIX and LTP are not significant, but they are negative and significant for the changes ΔVIX and ΔLTP. It means that the RF's performance deteriorates relative to the Bates model when market volatility or the risk of jumps rises from the training period to the time of forecast. This result is intuitive. Since the RF effectively fits a non-parametric volatility surface on the training data and then makes forecasts with it one week later, its performance will suffer if the level or the shape of the volatility surface changes significantly within the week. This is likely to happen when the market becomes more volatile or when the risk of jumps rises. The Bates model, although less flexible at fitting the volatility surface on any particular day, is more robust to changes in market conditions because it is designed to capture the dynamics of the underlying states.

Next, the Bates model performance deteriorates relative the RF for options with high bid-ask spreads, for short-dated options, and for deep OTM options. These results can be explained by the fact that the Bates model does not take into account the impact of market liquidity for option pricing, and it may require richer underlying dynamics (e.g., time-varying jump risks; see Andersen, Fusari, and Todorov, 2017) to price short-dated or deep OTM options. The flexibility of the RF model helps it better fit the data in such situations. Finally, the coefficient on the Mahalanobis Distance $D_{i,t}$ is also negative and

[18]The small difference in sample size between Table 5 and Table 4 is caused by the calculation of abnormal volume, $\widehat{Volume}_{i,t}$, which reduces the sample size slightly.

Table 5: **Panel Regression Results: Comparing MAE of Bates and RF Models.** This table presents the results from panel regressions comparing the mean absolute error (MAE) differences between the Bates and RF models for options pricing. The dependent variable is the difference in MAE between the two models for option i at time t. Independent variables include the VIX and its change (ΔVIX_t), LTP and its change (ΔLTP_t), relative bid-ask spread ($BidAsk_{i,t}$), a binary time-to-maturity indicator ($T_{i,t}^{1-7}$), and a binary out-of-money indicator ($OTM_{i,t}$). $D_{i,t}$ is the Mahalanobis distance between an option's strike price and time to maturity and the distribution of options at the time of calibration. Contract fixed effects are included. Standard errors are clustered at the date level. The sample period is from January 1996 to December 2019. The number of contract-day observations is 5,511,048.

	(1)	(2)	(3)	(4)	(5)	(6)
VIX_t	-1.2567**					-0.7313
	(0.5472)					(0.8255)
ΔVIX_t	-0.3035***					-0.2547***
	(0.0923)					(0.0961)
LTP_t		0.0568				0.0641
		(0.0805)				(0.1161)
ΔLTP_t		-0.7105***				-0.5096***
		(0.1433)				(0.1489)
$BidAsk_{i,t}$			1.1509***			0.4161***
			(0.0763)			(0.0813)
$T_{i,t}^{1-7}$				1.345***		1.3203***
				(0.0661)		(0.0707)
$OTM_{i,t}$				0.1029***		0.0511***
				(0.0166)		(0.015)
$D_{i,t}$					0.0016	-0.0422***
					(0.0131)	(0.0123)
Contract FE	Yes	Yes	Yes	Yes	Yes	Yes
Observations	5,511,048	5,511,048	5,511,048	5,511,048	5,511,048	5,511,048
R^2	0.132000	0.131900	0.132700	0.142800	0.130500	0.145300

significant after controlling for $T_{i,t}^{1-7}$ and $OTM_{i,t}$. It indicates that the relative performance of the Bates model improves when an option at time t has strike and time-to-maturity that are further away from the mass of the training sample. Intuitively, since interpolation by the non-parametric volatility surface becomes less reliable in regions where the training data is sparse, the RF's performance deteriorates in such cases.

Taken together, these results suggest that reduced-form models tend to outperform structural models when the latter are more severely misspecified, but reduced-form models

perform poorly when applied to data outside the training set.

4.4 Distribution of Option Returns

The last exercise we conduct with the surrogate model is to characterize the conditional distribution of option returns according to the Bates model and confront it with the data. Because option prices are nonlinear functions of the underlying state, characterizing the distribution of option returns typically requires simulating the state variables and then pricing the options under (a large number of) different realizations of the states. One would also use a similar procedure in simulated method of moment (SMM) estimations or when computing the Value-at-Risk of an option portfolio. We show that this procedure can be significantly expedited with the surrogate.

We follow Israelov and Kelly (2017) to model the dynamics of the underlying states using a vector autoregression (VAR). We denote the price of the underlying S&P500 index by S_t, and denote the first principle component of the implied volatility surface by PC_t. We then model the vector of states, which consists of S&P500 returns, the log VIX index, and the PC of the volatility surface, $X_t = \left[\frac{S_t}{S_{t-1}} - 1, \ln \text{VIX}_t, \text{PC}_t'\right]'$, as

$$X_t = \mu + \rho X_{t-1} + \Sigma_{t-1}\epsilon_t, \tag{26}$$

where the innovations ϵ_t are IID with mean zero and unit variance, and Σ_t is a diagonal matrix of GARCH$(1,1)$ volatilities. Israelov and Kelly (2017) model the volatility surface as driven by a factor model with static loadings on X_t and then price the options by interpolating the volatility surface. We also use the VAR and bootstrapped errors to forecast future changes in option moneyness and spot volatility, but price the options using the Bates model.

Specifically, we estimate the VAR in (26) on each day t using expanding windows with a minimum of 1000 observations. We then bootstrap M residuals which are fed into Eq. (26) to construct the forecast for day $t+1$,

$$\hat{X}^b_{t+1} = \hat{\mu} + \hat{\rho} X_t + \hat{\Sigma}_t \hat{\epsilon}^b_{t+1}, \quad b = 1, \cdots, M. \tag{27}$$

Using the same procedure, we can also obtain the forecast at longer horizon, $\hat{X}^b_{t+h}$. Next, we recover the forecast for instantaneous variance v_{t+h} in the Bates model by assuming that the change in log spot volatility is expected to be the same as that of the VIX index, so that $\sqrt{v^b_{t+h}} = \frac{VIX^b_{t+h}}{VIX_t}\sqrt{v_t}$.

Finally, we compute the bootstrapped BSIV of an option contract i at time $t+h$ as:

$$BSIV^b_{i,t+h} = \widehat{f}\left(s^b_{i,t+h}, \theta_t \mid \phi^*\right), \tag{28}$$

where $s^b_{i,t+h} = [m^b_{i,t+h}, \tau_i, v^b_{t+h}, r_{i,t}, d_{i,t}]$ (we keep the maturity-dependent risk-free rate and dividend yield at their values at time t), θ_t contains the parameters of the model estimated at time t, and $\widehat{f}$ denotes the deep surrogate. The BSIVs can then be readily converted into option prices and returns.

Any mismatch between the model-implied conditional distribution and the data could be due to one of the following reasons: 1) the VAR model for the underlying states could be misspecified; 2) parameter instability of the structural model; and 3) other misspecification of the structural model. We capture the mismatch as follows. For any option i on date t, we generate its conditional distribution of the price h days ahead using the bootstrap method above. Following Israelov and Kelly (2017), we examine how well this model-implied conditional distribution fits the data through quantile forecasts, that is, by checking the frequency with which the actual prices fall below the conditionally forecasted quantiles. For example, if the model is correct, the actual option prices on day $t+h$ should fall below the 50th percentile, which is generated based on information on day t, 50% of the time.

For ease of illustration, we choose three target tenors, with days-to-maturity of $\tau = [30, 60, 180]$, and five target levels of moneyness, $m = [-1.5, -1, -0.5, 0, 0.5]$. For each day, we group the options that deviate by less than 10% from the target tenor and moneyness into their corresponding category (15 groups in total). We then compute the forecasted quantiles for each option and report the percentage exceedance, that is, the percentage of option-days in the sample for which the predicted quantile exceeds the actual prices.

Panel A of Figure 9 reports the results for the Bates model. The forecasting horizon is one day. On the y-axis, we display the target quantile (black line) and the percentage exceedance.

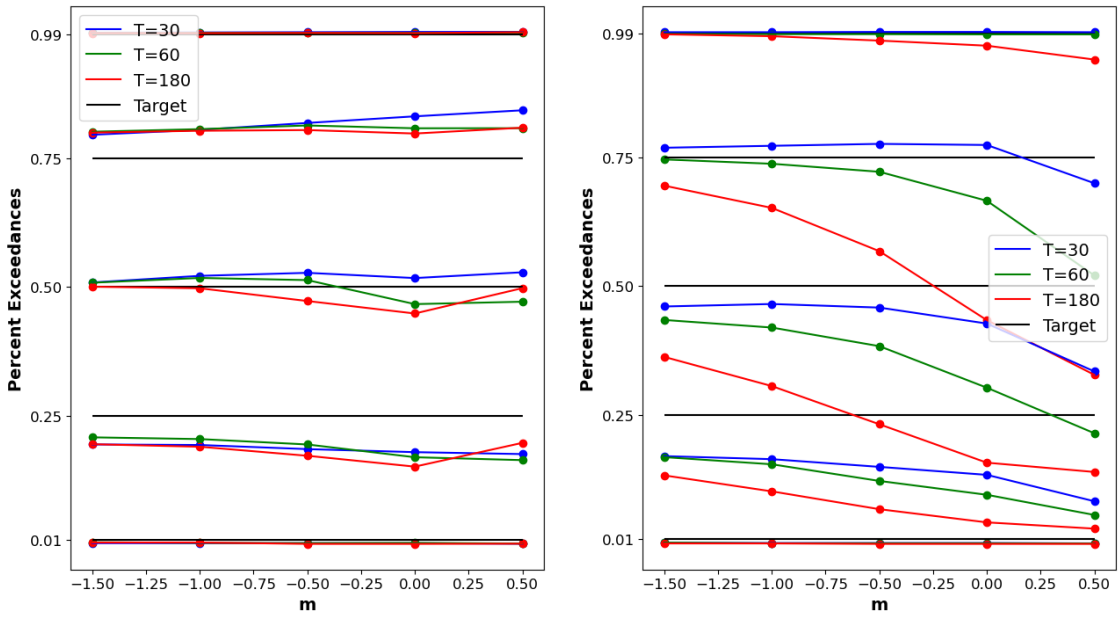

(a) Bates (b) Heston

Figure 9: **Quantile forecasts vs. the data.** The figures show the performances of the conditional option return distribution from the Bates model (a) and Heston model (b) based on the percentage exceedance at various target quantiles.

The blue, green, and red lines represent the three different target tenors. For each tenor, we show the percentage exceedance at the 1st, 25th, 50th, 75th, and 99th percentile across the five different target moneyness. For comparison, we conduct the same analysis for the stochastic volatility model by Heston (1993),[19] which does not feature jumps in the underlying asset. The results for the Heston model are reported in Panel B.

This test based on the conditional distribution of option returns is highly effective in demonstrating the limitations of the Bates model as well as its advantages over the Heston model. For the different target quantiles (especially at the 25th, 50th, and 75th percentile), the Bates model's percentage exceedance matches the target reasonably well. For the 25th percentile, the model-predicted quantile is likely too low, while the opposite is true for the 75th percentile, which could suggest more flexibility is needed in the Bates model when modeling the two sides of the jump distribution.

In contrast, across the quantiles, the percentage exceedance of the Heston model mostly falls short of the target at different maturity and moneyness. The shortfall is especially severe

[19]We build a separate deep surrogate for the Heston model for this exercise.

for longer-dated options, and for out-of-money calls. These issues are in part due to the fact that parameter instability is more severe for the Heston model, but they also reflect the Heston model's struggle to fit different parts of the volatility surface. The severe mismatch between the model-implied return distribution and the data has relevant consequences for practice. For example, the value-at-risk estimate for a portfolio of long-dated options based on the Bates model is likely to be significantly more accurate than one from the Heston model.

5 Conclusion

In this paper, we introduce *deep surrogates*: a generic framework to swiftly estimate complex structural models in economics and finance. We treat the model parameters as pseudo-state variables to create a deep neural network surrogate that replicates the target model. By alleviating the curse of dimensionality, this surrogate approach considerably reduces the computational cost for prediction and parameter estimation.

Our application, the estimation and analysis of a surrogate of the Bates option pricing model, illustrates how the *deep surrogate* methodology paves the way for a vast array of previously infeasible applications of structural models in finance and economics requiring including high-frequency re-estimation of parameters. In addition to enabling previously computationally infeasible analyses, deep surrogates can foster collaborations among academics. Indeed, trained surrogates can easily be shared by researchers, allowing others to utilize their model, thereby enhancing the accessibility and reproducibility of academic research.

References

Aldrich, E. M., J. Fernández-Villaverde, A. R. Gallant, and J. F. Rubio-Ramírez. 2011. Tapping the supercomputer under your desk: Solving dynamic equilibrium models with graphics processors. *Journal of Economic Dynamics and Control* 35:386–93.

Andersen, T. G., N. Fusari, and V. Todorov. 2015. Parametric inference and dynamic state recovery from option panels. *Econometrica* 83:1081–145.

———. 2017. Short-term market risks implied by weekly options. *The Journal of Finance* 72:1335–86.

Azinovic, M., L. Gaegauf, and S. Scheidegger. 2022. Deep equilibrium nets. *International Economic Review* n/a. doi:https://doi.org/10.1111/iere.12575.

Bach, F. 2017. Breaking the curse of dimensionality with convex neural networks. *Journal of Machine Learning Research* 18:1–53.

Bates, D. S. 1996. Jumps and stochastic volatility: Exchange rate processes implicit in deutsche mark options. *The Review of Financial Studies* 9:69–107.

———. 2000. Post-'87 crash fears in the S&P 500 futures option market. *Journal of Econometrics* 94:181–238.

Belkin, M., D. Hsu, and J. Xu. 2020. Two models of double descent for weak features. *SIAM Journal on Mathematics of Data Science* 2:1167–80.

Belkin, M., A. Rakhlin, and A. B. Tsybakov. 2019. Does data interpolation contradict statistical optimality? In *The 22nd International Conference on Artificial Intelligence and Statistics*, 1611–9. PMLR.

Berner, J., P. Grohs, and A. Jentzen. 2020. Analysis of the generalization error: Empirical risk minimization over deep artificial neural networks overcomes the curse of dimensionality in the numerical approximation of black–scholes partial differential equations. *SIAM Journal on Mathematics of Data Science* 2:631–57.

Bilionis, I., and N. Zabaras. 2012. Multidimensional adaptive relevance vector machines for uncertainty quantification. *SIAM Journal on Scientific Computing* 34:B881–908.

Black, F. 1976. Studies of stock price volatility changes. *In: Proceedings of the 1976 Meetings of the American Statistical Association* 171–81.

Black, F., and M. Scholes. 1973. The pricing of options and corporate liabilities. *Journal of political economy* 81:637–54.

Bollerslev, T., and V. Todorov. 2011. Tails, fears, and risk premia. *The Journal of Finance* 66:2165–211. doi:10.1111/j.1540-6261.2011.01695.x.

Bollerslev, T., V. Todorov, and L. Xu. 2015. Tail risk premia and return predictability. *Journal of Financial Economics* 118:113–34.

Breiman, L. 2001. Random forests. *Machine Learning* 45:5–32.

Brumm, J., and S. Scheidegger. 2017. Using adaptive sparse grids to solve high-dimensional dynamic models. *Econometrica* 85:1575–612. ISSN 1468-0262. doi:10.3982/ECTA12216.

Chen, H., Y. Cheng, Y. Liu, and K. Tang. 2024. Teaching economics to the machines. Working Paper, MIT.

Chen, H., W. W. Dou, and L. Kogan. 2022. Measuring "dark matter" in asset pricing models. *Journal of Finance*, forthcoming.

Chen, H., and S. Joslin. 2012. Generalized Transform Analysis of Affine Processes and Applications in Finance. *Review of Financial Studies* 25:2225–56.

Chen, L., M. Pelger, and J. Zhu. 2023. Deep learning in asset pricing. *Management Science* .

Chen, P., N. Zabaras, and I. Bilionis. 2015. Uncertainty propagation using infinite mixture of gaussian processes and variational bayesian inference. *Journal of computational physics* 284:291–333.

Chen, X., and H. White. 1999. Improved rates and asymptotic normality for nonparametric neural network estimators. *IEEE Transactions on Information Theory* 45:682–91.

Christoffersen, P., and K. Jacobs. 2004. The importance of the loss function in option valuation. *Journal of Financial Economics* 72:291 – 318. ISSN 0304-405X. doi:https://doi.org/10.1016/j.jfineco.2003.02.001.

Deisenroth, M. P., C. E. Rasmussen, and J. Peters. 2009. Gaussian process dynamic programming. *Neurocomputing* 72:1508–24.

Duarte, V., D. Duarte, and D. Silva. 2023. Machine learning for continuous-time economics Working paper.

Duffie, D., J. Pan, and K. Singleton. 2000. Transform analysis and asset pricing for affine jump-diffusions. *Econometrica* 68:1343–76. doi:10.1111/1468-0262.00164.

Farrell, M. H., T. Liang, and S. Misra. 2021. Deep neural networks for estimation and inference. *Econometrica* 89:181–213–. ISSN 0012-9682. doi:10.3982/ecta16901.

Fernández-Villaverde, J., S. Hurtado, and G. Nuño. 2023. Financial frictions and the wealth distribution. *Econometrica* 91:869–901.

Fernández-Villaverde, J., J. Rubio-Ramírez, and F. Schorfheide. 2016. None. vol. 2 of *Handbook of Macroeconomics*, 527 – 724. Elsevier. doi:https://doi.org/10.1016/bs.hesmac.2016.03.006.

Friedl, A., F. Kübler, S. Scheidegger, and T. Usui. 2023. Deep uncertainty quantification: With an application to integrated assessment models. Working paper, University of Lausanne.

Gao, J., and J. Pan. 2023. Option-implied crash index. Working Paper.

Goodfellow, I., Y. Bengio, A. Courville, and Y. Bengio. 2016. *Deep learning*, vol. 1. MIT press Cambridge.

Grohs, P., F. Hornung, A. Jentzen, and P. von Wurstemberger. 2023. A proof that artificial neural networks overcome the curse of dimensionality in the numerical approximation of black–scholes partial differential equations. *Memoirs of the American Mathematical Society* 284.

Gu, S., B. Kelly, and D. Xiu. 2018. Empirical asset pricing via machine learning. Working Paper, National Bureau of Economic Research.

Gühring, I., M. Raslan, and G. Kutyniok. 2020. Expressivity of deep neural networks. *arXiv preprint arXiv:2007.04759* .

Hall, A. R., and A. Inoue. 2003. The large sample behaviour of the generalized method of moments estimator in misspecified models. *Journal of Econometrics* 114:361–94.

Han, J., Y. Yang, et al. 2021. Deepham: A global solution method for heterogeneous agent models with aggregate shocks. Working Paper, arXiv preprint arXiv:2112.14377.

Hanin, B. 2019. Universal function approximation by deep neural nets with bounded width and ReLU activations. *Mathematics* 7:992–.

Hansen, B. E., and S. Lee. 2021. Inference for iterated gmm under misspecification. *Econometrica* 89:1419–47.

Hansen, L. P. 1982. Large sample properties of generalized method of moments estimators. *Econometrica* 50:1029–54.

Heiss, F., and V. Winschel. 2008. Likelihood approximation by numerical integration on sparse grids. *Journal of Econometrics* 144:62 – 80. ISSN 0304-4076. doi:https://doi.org/10.1016/j.jeconom.2007.12.004.

Heston, S. L. 1993. A closed-form solution for options with stochastic volatility with applications to bond and currency options. *The review of financial studies* 6:327–43.

Hochreiter, S. 1998. The vanishing gradient problem during learning recurrent neural nets and problem solutions. *International Journal of Uncertainty, Fuzziness and Knowledge-Based Systems* 6:107–16.

Hornik, K., M. Stinchcombe, and H. White. 1989. Multilayer feedforward networks are universal approximators. *Neural networks* 2:359–66.

Hutchinson, J. M., A. W. Lo, and T. Poggio. 1994. A nonparametric approach to pricing and hedging derivative securities via learning networks. *The Journal of Finance* 49:851–89.

Israelov, R., and B. T. Kelly. 2017. Forecasting the distribution of option returns. *Available at SSRN 3033242* .

Kaji, T., E. Manresa, and G. Pouliot. 2020. An Adversarial Approach to Structural Estimation. *arXiv e-prints* arXiv:2007.06169.

Kase, H., L. Melosi, and M. Rottner. 2022. Estimating nonlinear heterogeneous agents models with neural networks. *Available at SSRN 4138711* .

Krause, A., and C. Guestrin. 2007. Nonmyopic active learning of gaussian processes: an exploration-exploitation approach. In *Proceedings of the 24th international conference on Machine learning*, 449–56.

Liaw, A., M. Wiener, et al. 2002. Classification and regression by randomforest. *R news* 2:18–22.

Liu, S., A. Borovykh, L. A. Grzelak, and C. W. Oosterlee. 2019. A neural network-based framework for financial model calibration. *Journal of Mathematics in Industry* 9:9–.

Maliar, L., S. Maliar, and P. Winant. 2021. Deep learning for solving dynamic economic models. *Journal of Monetary Economics* 122:76–101. ISSN 0304-3932. doi:https://doi.org/10.1016/j.jmoneco.2021.07.004.

Montanelli, H., and Q. Du. 2019. New error bounds for deep relu networks using sparse grids. *SIAM Journal on Mathematics of Data Science* 1:78–92.

Montanelli, H., H. Yang, and Q. Du. 2021. Deep relu networks overcome the curse of dimensionality for generalized bandlimited functions. *Journal of Computational Mathematics* 39:801–15.

Norets, A. 2012. Estimation of dynamic discrete choice models using artificial neural network approximations. *Econometric Reviews* 31:84–106. doi:10.1080/07474938.2011.607089.

Pan, J. 2002. The jump-risk premia implicit in options: evidence from an integrated time-series study. *Journal of Financial Economics* 63:3–50.

Park, J., and I. W. Sandberg. 1991. Universal approximation using radial-basis-function networks. *Neural computation* 3:246–57.

Payne, J., A. Rebei, and Y. Yang. 2024. Deep learning for search and matching models. Available at SSRN 4768566.

Petersen, P., and F. Voigtlaender. 2018. Optimal approximation of piecewise smooth functions using deep relu neural networks. *Neural Networks* 108:296–330. ISSN 0893-6080. doi:https://doi.org/10.1016/j.neunet.2018.08.019.

Ramachandran, P., B. Zoph, and Q. V. Le. 2017. Swish: a self-gated activation function. *arXiv: Neural and Evolutionary Computing* .

Ren, P., Y. Xiao, X. Chang, P.-Y. Huang, Z. Li, B. B. Gupta, X. Chen, and X. Wang. 2021. A survey of deep active learning. *ACM computing surveys (CSUR)* 54:1–40.

Renner, P., and S. Scheidegger. 2018. Machine learning for dynamic incentive problems. *Available at SSRN 3282487* .

Schaefer, S. M., and I. A. Strebulaev. 2008. Structural models of credit risk are useful: Evidence from hedge ratios on corporate bonds. *Journal of Financial Economics* 90:1 – 19. ISSN 0304-405X. doi:https://doi.org/10.1016/j.jfineco.2007.10.006.

Scheidegger, S., and I. Bilionis. 2019. Machine learning for high-dimensional dynamic stochastic economies. *Journal of Computational Science* 33:68 – 82. ISSN 1877-7503. doi:https://doi.org/10.1016/j.jocs.2019.03.004.

Scheidegger, S., D. Mikushin, F. Kubler, and O. Schenk. 2018. Rethinking large-scale economic modeling for efficiency: Optimizations for gpu and xeon phi clusters. In *2018 IEEE International Parallel and Distributed Processing Symposium (IPDPS)*, 610–9. ISSN 1530-2075. doi:10.1109/IPDPS.2018.00070.

Scheidegger, S., and A. Treccani. 2018. Pricing American Options under High-Dimensional Models with Recursive Adaptive Sparse Expectations*. *Journal of Financial Econometrics* ISSN 1479-8409. doi:10.1093/jjfinec/nby024. Nby024.

Traub, J. F., and A. G. Werschulz. 1998. *Complexity and information*, vol. 26862. Cambridge University Press.

Tripathy, R., I. Bilionis, and M. Gonzalez. 2016. Gaussian processes with built-in dimensionality reduction: Applications to high-dimensional uncertainty propagation. *Journal of Computational Physics* 321:191–223.

Tripathy, R. K., and I. Bilionis. 2018. Deep uq: Learning deep neural network surrogate models for high dimensional uncertainty quantification. *Journal of Computational Physics* 375:565 – 588. ISSN 0021-9991. doi:https://doi.org/10.1016/j.jcp.2018.08.036.

Villa, A. T., and V. Valaitis. 2019. Machine learning projection methods for macro-finance models. *Economic Research Initiatives at Duke (ERID) Working Paper* .

Williams, C. K., and C. E. Rasmussen. 2006. *Gaussian processes for machine learning*, vol. 2. MIT press Cambridge, MA.

Appendix

A Surrogate Construction

In this section, we discuss several considerations in the construction of the deep surrogate. First, Table A.1 shows the ranges of parameters used to generate the simulated samples for training the Bates and Heston surrogates, as described in Section 3.2.

Table A.1: This table presents the ranges for the surrogate model of the Heston model and Bates's training sample. To create the surrogate models, we generate sample options. We first draw the option parameters, states, and hidden states from uniform distributions, and then use the original model to price those options. The table below shows the minimum and maximum values of these uniform distributions. The first two columns show the minimum and maximum values of the uniform distributions used to generate the Heston Model, while the last two columns show the same values for the Bates model.

j	Heston: $\underline{x}^{(j)}$	Heston: $\bar{x}^{(j)}$	Bates: $\underline{x}^{(j)}$	Bates: $\bar{x}^{(j)}$
m	-9.00	5.000	-9.00	5.000
rf	0.00	0.075	0.00	0.075
dividend	0.00	0.050	0.00	0.050
v_t	0.01	0.900	0.01	0.900
T	1.00	365.000	1.00	365.000
κ	0.10	50.000	0.10	50.000
$\bar{v}$	0.01	0.900	0.01	0.900
σ	0.10	5.000	0.10	5.000
ρ	-	-	-1.00	-0.000
λ	-	-	0.00	4.000
ν_1	-	-	0.00	0.400
ν_2	-	-	0.00	0.400
p	-	-	0.00	1.000

Figure A.1 illustrates the low risk of overfitting by showing the errors in the training of a simple surrogate of the Black-Scholes model (Black and Scholes, 1973). The surrogate model has 4 hidden layers with 400 Swish-activated neurons each. We use a small training sample of 10,000 simulated options. This choice reduces the cost of training the model for 1,000 epochs but also illustrates that overfitting is unlikely to occur even with a small sample. Indeed, we see that both the in-sample performance (measured on the training sample) and the out-of-sample error (measured on a validation sample of 10,000 simulated options not seen during training) do not show signs of overfitting, even as we let the optimization run for 1,000 epochs.

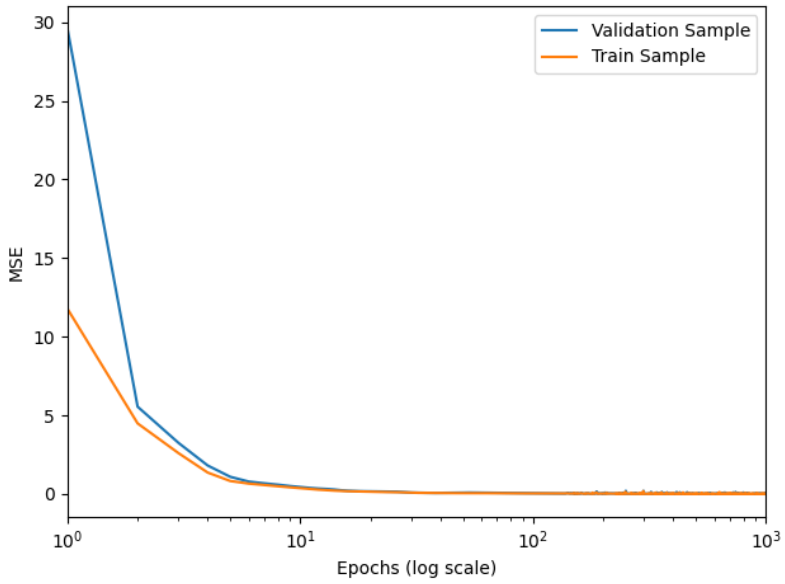

Figure A.1: **Training Error: Black-Scholes Surrogate.** This figure shows the mean square error of the Black-Scholes surrogate throughout training. The training error is computed across epochs and averaged for each batch. The validation error is based on a sample of 10,000 simulated options not seen during training. To reduce computational cost from running the model for 1,000 epochs, we train a surrogate of the Black-Scholes model with 5 hidden layers (400 neurons with the Swish activation function in each layer) and only 10,000 training samples.

B Surrogate Accuracy

In this appendix, we expand on the analysis in Section 3.3 to further examine parameter estimation errors and their minimal impact on option pricing errors.

First, Table A.2 show the average true BSIV (Panel A) and option Delta (Panel B) for the options in the 12 maturity-moneyness bins used to examine the deep surrogate's accuracy in Section 3.3. They serve as benchmarks to help us gauge the magnitude of the absolute pricing errors in Figure 1 and Delta errors in Figure 2.

We follow steps 1, 2, and 3 of the procedure described in Section 3.3 to generate Figure 3, which evaluates the accuracy of the deep surrogate in estimating the parameters of the Bates model from data. Next, we define a relative estimation error measure,

$$e_i = \frac{|\hat{\theta}_i^{DS} - \theta_i|}{\epsilon + |\theta_i|}, \tag{A.1}$$

where $\hat{\theta}_i^{DS}$ is the GMM estimate of the i-th parameter through the deep surrogate and θ_i is the true value. The positive constant helps avoid exploding errors when the true parameter

Table A.2: Summary statistics of the simulated options. Panel A shows the average implied volatility ($BSIV_{true}$) across 12 bins, while Panel B shows the average Delta across the same bins.

A. Average Implied Volatility ($BSIV_{true}$)

	$\tau \leqslant 7$	$7 < \tau \leqslant 30$	$30 < \tau \leqslant 90$	$\tau < 90$
Low m	0.671	0.702	0.702	0.681
Mid m	0.520	0.562	0.592	0.621
High m	0.548	0.587	0.618	0.641

B. Average Delta

	$\tau \leqslant 7$	$7 < \tau \leqslant 30$	$30 < \tau \leqslant 90$	$\tau < 90$
Low m	0.947	0.941	0.937	0.932
Mid m	0.703	0.704	0.703	0.711
High m	0.208	0.224	0.249	0.298

value is close to zero. One weakness of this new measure is that the size of the constant ϵ is arbitrary. In cases where $|\theta_i| \gg \epsilon$, e_i can be viewed as approximately the relative estimation error.

Figure A.2 presents the results, where we set the constant $\epsilon = 0.1$. The relative estimation errors are small in most cases. For all parameters and the volatility state v_t, the 75th percentile of the relative estimation error is below 3%. However, for λ, p, ρ, and σ, the relative errors can be higher in the tails.

Why are the relative estimation errors larger for some of the parameters, and why these estimation errors do not appear to cause more significant pricing errors out of sample, as shown in Figure 3? Since the estimation is done with option pricing data that are "observed" without error, provided that we use the correctly specified model and that the standard identification assumptions are satisfied, we should be able to recover the true parameter values perfectly.[20] Thus, the estimation errors shown in Figure A.2 are primarily caused by the approximation errors of the deep surrogate.

Let us now consider two cases: one where the option price (BSIV) exhibits low sensitivity to changes in parameter values, and another where the sensitivity is high. These cases are illustrated in Figure A.3. The differences in sensitivities are evident from the slopes of the true prices P (blue lines) as functions of the parameter value θ in the two panels. The red lines represent the deep surrogate solutions, closely mimicking the true solutions. The

[20]This is subject to the numerical errors when computing option prices via FFT and the errors with searching for parameters to minimize the GMM objective.

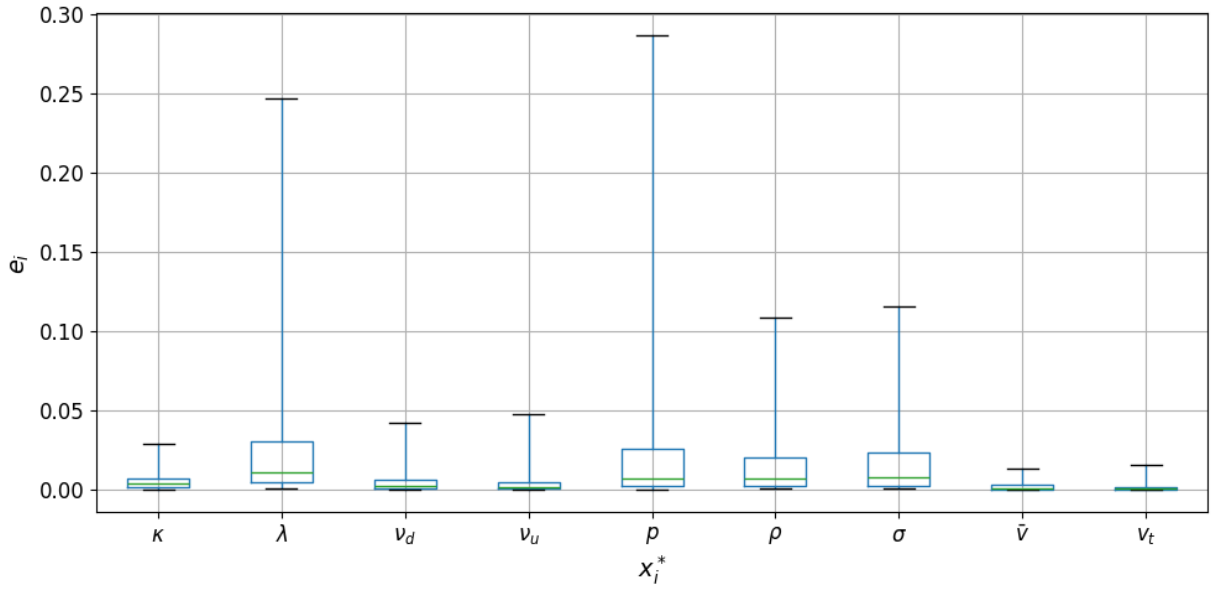

Figure A.2: **Structural Estimation via the Deep Surrogate.** This figure illustrates the accuracy of estimating the hidden state and parameters of the Bates model using the deep surrogate. Boxplots summarize the estimation errors for the hidden state v_t and model parameters, based on 1,000 simulations with samples of 1,000 options each. The interquartile range is shown within the box, while the whiskers indicate the 5th and 95th percentiles of the estimation error distribution across simulations.

gaps between the red and blue lines indicate the approximation errors of the deep surrogate. Notably, the average approximation errors are consistent between the low- and high-sensitivity cases.

Now suppose the observed option price is $P(\theta_0)$. Under the true pricing function, the parameter value θ_0 can be recovered accurately, regardless of the sensitivity of the pricing function. When estimating θ using the deep surrogate, approximation errors result in the estimate $\hat{\theta}$. Comparing Panels A and B of Figure A.3, we observe that under low sensitivity of P to θ, even small approximation errors in the pricing function can lead to significant parameter estimation errors, $|\hat{\theta} - \theta_0|$. This scenario resembles "weak identification," where minor model misspecification causes substantial inference errors. However, despite the significantly larger parameter estimation error in Panel A, the pricing errors, $|P(\hat{\theta}) - P(\theta_0)|$, evaluated using the true pricing function (blue lines), are comparable between the two panels. This occurs because the lower sensitivity of P to θ in Panel A offsets the larger discrepancy between $\hat{\theta}$ and θ_0.

In summary, the differences in the sensitivity of option prices to individual parameters explain the variations in the range of estimation errors across parameters observed in Figure A.2. Specifically, the results highlight that option prices are relatively less sensitive to

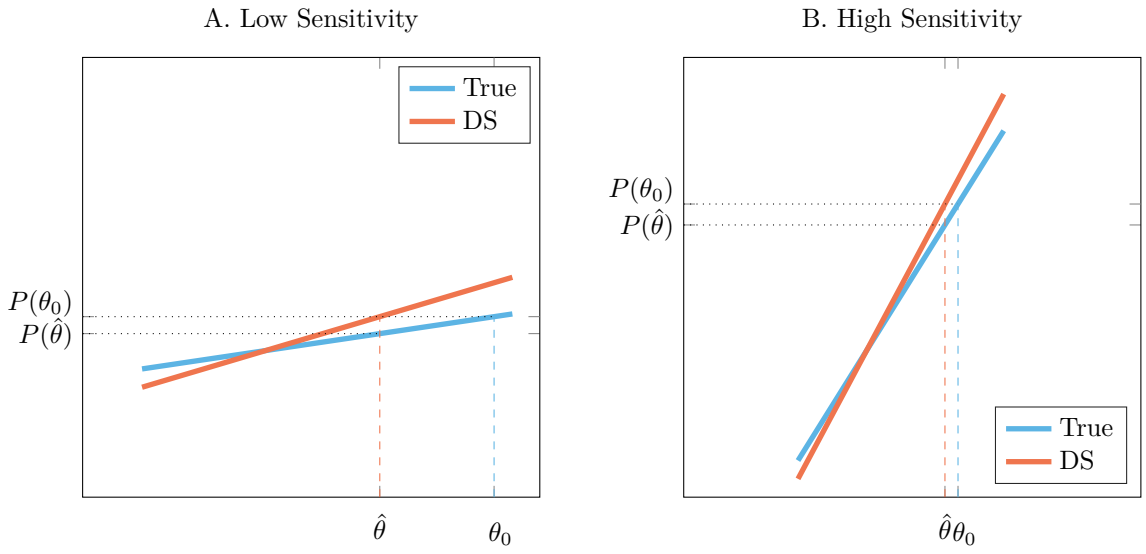

Figure A.3: **Relationship between Parameter Estimation Error and OOS Pricing Error.** The blue lines depict the true pricing function, while the red lines show the solutions obtained using the deep surrogate.

changes in λ, p, ρ, and σ. Nevertheless, the high accuracy of the deep surrogate ensures that, even when some parameters are estimated with errors, these errors have minimal economic consequences, as reflected in the pricing errors. This observation accounts for the consistently small out-of-sample pricing errors shown in Figure 3.

C Data Sample

Figure A.4 provides a summary of our sample. Panel A shows the evolution of the distribution of time-to-maturity for the SPX options. Panel B shows a dramatic increase in the number of SPX options traded in the past decade (left axis). The percentage of put options in the sample (right axis) exceeds 50% most of the time and has risen above 70% in the past decade.

D Black Scholes Surrogate

In this appendix, we use the Black-Scholes model (Black and Scholes, 1973) to compare the performance of surrogate models employing *ReLU* and *swish* activation functions.

The Black-Scholes model is considerably simpler than the Bates model for two reasons: it can be solved in closed form, and it involves fewer parameters and states. This significantly reduces the cost of training surrogate models, both by lowering the cost of data generation and

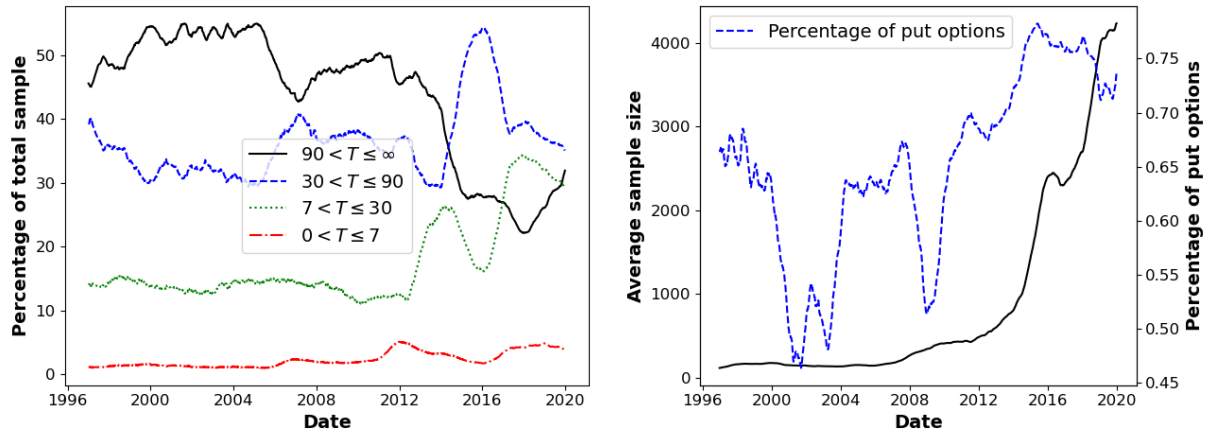

(a) Maturities in sample

(b) Number of options

Figure A.4: **Sample Summary Statistics.** The figures above depict the evolution of the sample composition over time. Panel (a) illustrates the percentage of options in the sample across different maturity brackets. Panel (b) shows the total number of options per day (left axis) and the percentage of put options in the sample (right axis). All results are smoothed using a rolling average over the past 252 business days.

by decreasing the required complexity of the network. These properties make it well-suited for experiments that highlight the characteristics of surrogate models.

In our first experiment, we compare the accuracies of two surrogates for the Black-Scholes model in predicting option prices and Deltas. The two surrogates share the same architecture (5 layers with 400 neurons each) and differ only in their activation functions.[21] The results are presented in Figure A.5 and Figure A.6, respectively. As shown, the choice of activation function has a relatively small impact on the accuracy of option prices. However, for option Deltas, the surrogate with Swish activation consistently outperforms the one with ReLU across different maturities and levels of moneyness.

Next, we use Figure A.7 to further illustrate how the ReLU-surrogate struggles to match the option Delta. As moneyness (Panel c) and volatility (Panel d) vary along the x-axis, the Swish-surrogate consistently aligns with the Delta from the closed-form solution. In contrast, the ReLU-surrogate occasionally produces significant errors, evident in the spikes along the solid line.

[21] All other hyperparameters are kept constant across the two networks: batch size of 256, initial learning rate of 0.001, ADAM optimizer, and 100 million simulated training samples.

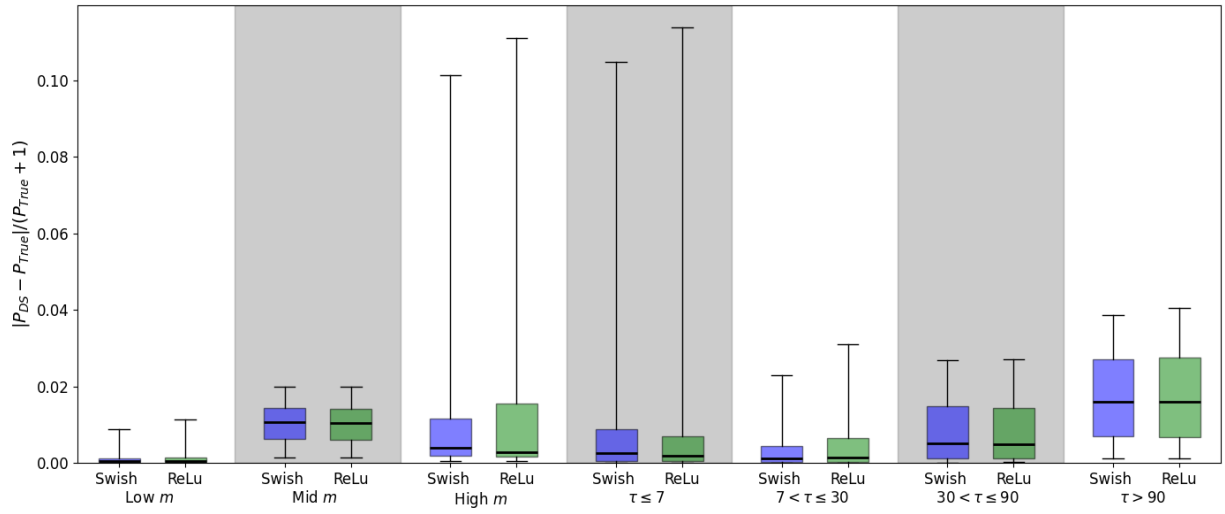

Figure A.5: **Black-Scholes Prices: *ReLU* vs *Swish*.** This figure illustrates the impact of changing the activation function from *ReLU* to *Swish*. Each boxplot corresponds to a surrogate model with identical architecture and hyperparameters: 5 hidden layers with 400 neurons per layer, a batch size of 256, the ADAM optimizer with an initial learning rate of 0.001, and a training sample of 100 million simulated observations. The only difference between the models is the activation function used. In each bracket, the left blue boxplot represents the *Swish* activation function, while the right green boxplot represents the *ReLU* activation function. The y-axis denotes the pricing error, normalized by the *true* price plus 1 (to prevent numerical issues with prices close to zero). The true price is computed using the closed-form Black-Scholes formula. The pricing error distribution is estimated on a random sample of 20,000 options, generated for each combination of m and T terciles. Each box represents the interquartile range, with whiskers indicating the 5th and 95th percentiles of the estimation error distribution across simulations.

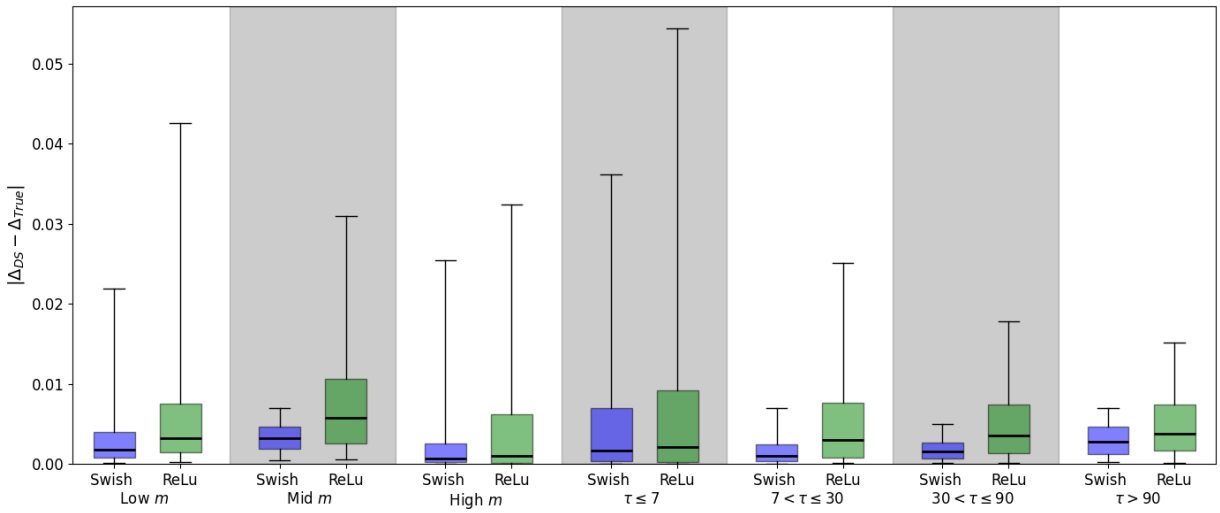

Figure A.6: **Black-Scholes Delta: *ReLU* vs *Swish*.** This figure expands on the results presented in Figure A.5. We repeat the same procedure to show the surrogate's estimation error of the options Delta.

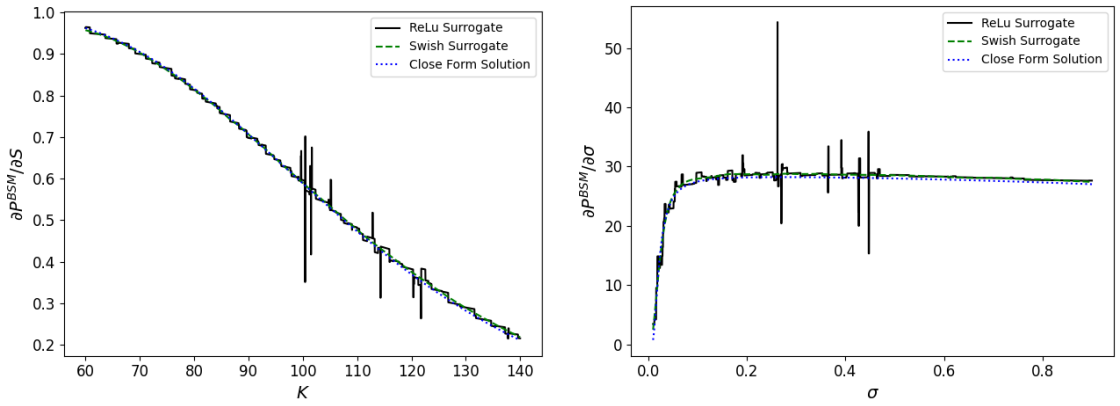

(a) (b)

Figure A.7: ***ReLU* Effect on Surrogate Delta.** The figures compare the first derivative of the Black-Scholes model (BSM) surrogate using a Swish activation function with that of a surrogate using a ReLU activation function, as well as the true values obtained from the closed-form BSM solution. The state space is populated with points where all parameters and states are fixed at their mid-range values: $\hat{K} = 100.0$, $r = 0.0375$, $T = 190$, $\kappa = 25.05$, $v_t = 0.455$, and $d = 0.0375$. In the first column, the x-axis represents the volatility parameter v_t, varied between the minimum and maximum values of the surrogate state space. In the second column, the x-axis represents the time-to-maturity parameter T, varied between its minimum and maximum values in the surrogate state space.